HHS Public Access

Author manuscript

Nat Metab. Author manuscript; available in PMC 2023 November 29.

Published in final edited form as:

Nat Metab. 2023 August ; 5(8): 1382–1394. doi:10.1038/s42255-023-00844-5.

CRAT links cholesterol metabolism to innate immune responses in the heart

Hua Mao[1,2,6], **Aude Angelini**[1,2,6], **Shengyu Li**[3,4,6], **Guangyu Wang**[3,4], **Luge Li**[1,2], **Cam Patterson**[5], **Xinchun Pi**[1,2], **Liang Xie**[1,2]

[1]Department of Medicine, Section of Cardiovascular Research, Baylor College of Medicine, Houston, TX, USA.

[2]Cardiovascular Research Institute, Baylor College of Medicine, Houston, TX, USA.

[3]Center for Cardiovascular Regeneration, Houston Methodist Research Institute, Houston, TX, USA.

[4]Department of Cardiothoracic Surgery, Weill Cornell Medicine, Cornell University, New York, NY, USA.

[5]University of Arkansas for Medical Sciences, Little Rock, AR, USA.

[6]These authors contributed equally: Hua Mao, Aude Angelini, Shengyu Li.

Abstract

Chronic inflammation is associated with increased risk and poor prognosis of heart failure; however, the precise mechanism that provokes sustained inflammation in the failing heart remains elusive. Here we report that depletion of carnitine acetyltransferase (CRAT) promotes cholesterol catabolism through bile acid synthesis pathway in cardiomyocytes. Intracellular accumulation of bile acid or intermediate, 7α-hydroxyl-3-oxo-4-cholestenoic acid, induces mitochondrial DNA stress and triggers cGAS–STING-dependent type I interferon responses. Furthermore, type I interferon responses elicited by CRAT deficiency substantially increase AIM2 expression and AIM2-dependent inflammasome activation. Genetic deletion of cardiomyocyte CRAT in mice of both sexes results in myocardial inflammation and dilated cardiomyopathy, which can be reversed by combined depletion of caspase-1, cGAS or AIM2. Collectively, we identify a mechanism by which cardiac energy metabolism, cholesterol homeostasis and cardiomyocyte-intrinsic innate immune responses are interconnected via a CRAT-mediated bile acid synthesis pathway, which contributes to chronic myocardial inflammation and heart failure progression.

Correspondence and requests for materials should be addressed to Liang Xie. liangx@bcm.edu.

Author contributions

L.X. and X.P. conceived and designed the studies. H.M., A.A., L.L., C.P., X.P. and L.X. performed the experiments and interpreted data. G.W. and S.L. performed the RNA-seq analysis. L.X. and X.P. co-wrote the manuscript. L.X. carried out experimental design and interpretation and supervised the project. All authors approved the manuscript.

Competing interests

The authors declare no competing interests.

Extended data is available for this paper at https://doi.org/10.1038/s42255-023-00844-5.

Supplementary information The online version contains supplementary material available at https://doi.org/10.1038/s42255-023-00844-5.

Heart failure (HF), a complex clinical syndrome resulting from impaired cardiac function, remains the leading cause of morbidity and mortality across the globe, imposing an enormous clinical and economic burden[1]. Despite substantial progress in understanding the pathogenesis of HF, current therapies are largely focused on the inhibition of neurohormonal activation and the prognosis for patients with HF remains poor[2]. Thus, there is an urgent need for new therapies to improve cardiac performance and prevent the deleterious cardiac remodeling in patients with HF. Emerging evidence suggests that disturbance in cardiomyocyte (CM) metabolism contributes to the progression of HF[3]. CRAT is a mitochondrial enzyme and catalyzes the conversion of acetyl-CoA to acetylcarnitine, which enables its export from mitochondria. CRAT plays a central role in regulating metabolic flexibility and promoting substrate switching from fatty acid to glucose in skeletal myocytes[4]. Of note, CRAT is most abundantly expressed in the heart and its activity is dramatically decreased in a mouse model of HF[4,5]; however, whether dysregulation of this enzyme contributes to the pathogenesis of HF remains largely uncharacterized.

Results

Deletion of CRAT in CMs leads to dilated cardiomyopathy

To verify whether CRAT expression is altered in patients with HF, we performed single-cell RNA-sequencing (scRNA-seq) analysis with dataset obtained from the original publication under Gene Expression Omnibus (GEO) accession nos. GSE109816 and GSE121893 (ref. 6). *t*-distributed stochastic neighbor embedding (*t*-SNE) clustering of 9,248 single cells isolated from both healthy and HF hearts revealed five major cell types, including CMs, endothelial cells, fibroblasts (FBs), macrophages (MPs) and smooth muscle cells (Fig. 1a). CRAT was most abundantly expressed in CMs and its expression was significantly downregulated in both CMs and FBs from patients with HF (Fig. 1b,c). It was reported that CRAT activity was reduced in a mouse model of HF[5]. Consistently, although we observed no significant change in CRAT protein level, we demonstrated that CRAT activity was dramatically decreased in mouse failing hearts caused by transaortic constriction (TAC) (Fig. 1d-f).

To demonstrate the specific role of CM CRAT in heart function, we generated *Crat* (flox/flox); Myh6-MerCreMer^{+} (CRAT-mKO) mice to specifically delete CRAT in CMs by injection of tamoxifen. Consistent with a previous report[7], we did not observe any Cre-dependent deleterious effect on cardiac function and induction of hypertrophic or profibrotic genes in Myh6-MerCreMer^{+} mice after injection of low doses of tamoxifen (Extended Data Fig. 1a-f). Therefore, we used *Crat* (flox/flox); Myh6-MerCreMer^{-} (CRAT-WT) littermate mice as the controls for CRAT-mKO mice. Analyses with western blot and enzymatic activity assay confirmed the loss of CRAT in the hearts but not in other tissues of CRAT-mKO mice (Extended Data Fig. 2a,b). It was reported that knockout of CRAT led to an increase in acetyl-CoA levels[8]. Consistently, we observed a significant increase in acetyl-CoA levels in CRAT-mKO hearts (Extended Data Fig. 2c). In addition, we found that deletion of CRAT in CMs led to significant increases in heart weight (HW):body weight (BW) and HW:tibia length (TL) ratios (Fig. 2a-c). Significant decreases in ejection fraction and fractional shortening and increase in left ventricular chamber size were also evident in

CRAT-mKO mice (Fig. 2d-g). Furthermore, wheat germ agglutinin (WGA) staining revealed a dramatic increase in CM cross sectional size, suggesting a trend toward hypertrophy for CRAT-deficient CMs (Fig. 2h). Consistent with these changes, we observed marked induction of hypertrophy marker genes in CRAT-mKO hearts (Fig. 2i). Finally, Masson's trichrome staining indicated the presence of severe interstitial fibrosis in CRAT-mKO hearts, accompanied by significant increases in the expression of key profibrotic genes (Fig. 2j,k). Taken together, these data show that CM-specific deletion of CRAT impairs cardiac function and results in dilated cardiomyopathy (DCM).

Depletion of CRAT triggers type I interferon responses

To uncover the underlying mechanism by which CRAT deficiency impairs cardiac function, we first examined whether depletion of CRAT directly provoked hypertrophic or profibrotic responses in cultured CMs in vitro. Notably, knockdown of CRAT in primary neonatal rat ventricular CMs (NRVMs) had no effect or even decreased the expression of hypertrophic or profibrotic genes (Extended Data Fig. 3a-f). Instead, we observed significant increases in the expression of proinflammatory cytokines, such as interleukin (IL)-1β, IL-6 and tumor necrosis factor (TNF)-α, in CRAT-deficient NRVMs (Extended Data Fig. 3g-i). To characterize the potential inflammatory pathways induced by CRAT deficiency, we performed RNA-sequencing (RNA-seq) analysis. Gene expression profiling of CRAT-deficient NRVMs revealed an unexpected enrichment of interferon-stimulated genes (ISGs) (Fig. 3a,b). Notably, we observed a dramatic increase in the expression of cytoplasmic RNA or DNA sensors, such as *Ddx58*, *Ifih1* and *Aim2*, suggesting that CRAT deficiency may induce cytosolic nucleic acid stress. The increased expression of ISGs was further confirmed by PCR with reverse transcription (RT–PCR) and western blot (Fig. 3c-i and Extended Data Fig. 4a-e). To determine whether the type I interferon responses induced by CRAT deficiency were unique to CMs, we also knocked down the expression of CRAT in cardiac FBs and observed similar increases in ISG expression (Extended Data Fig. 5a-d), suggesting that a conserved mechanism is involved in the type I interferon responses induced by CRAT deficiency in different cell types.

We next examined whether cyclic GMP-AMP synthase (cGAS) was responsible to the increased expression of ISGs, as the cGAS–STING pathway has emerged as a key pathway that detects aberrant intracellular DNA[9]. Not surprisingly, we demonstrated that knockdown of cGAS largely abrogated ISG expression in CRAT-deficient NRVMs (Fig. 3d-i). Accumulative evidence suggests that mitochondrial stress promotes the release of mitochondrial DNA (mtDNA) fragments into cytosol via the mitochondrial permeability transition pore (mPTP), where they trigger the type I interferon responses through the cGAS–STING pathway[10-13]. Thus, we examined whether depletion of CRAT induced mtDNA release into the cytosol and found that cytosolic mtDNA (cmtDNA) levels were significantly higher in CRAT-deficient NRVMs than in control cells, despite having similar levels of total mtDNA (Fig. 3j and Extended Data Fig. 6a,b). Similar results were also obtained from adult CMs isolated from CRAT-WT or CRAT-mKO mice (Fig. 3k and Extended Data Fig. 6c). In addition, treatment with cyclosporin A (CsA), a mPTP inhibitor that has been shown to inhibit mtDNA fragment release into cytosol[10,12], dramatically inhibited ISG expression in CRAT-deficient NRVMs (Fig. 3l). Collectively, we demonstrated

that depletion of CRAT promotes mtDNA release into cytosol via mPTP and triggers the cell-intrinsic type I interferon responses in CMs.

7-HOCA promotes mtDNA stress and induces ISG expression

mtDNA exists as a circular double-stranded DNA molecule that is packaged into higher-order structures called nucleoids[14]. Defects in mtDNA replication and packaging or various endogenous and exogenous stress such as reactive oxygen species often lead to the loss of mtDNA integrity and increased accumulation of cytosolic mtDNA fragments[11-13,15]. Deletion of CM CRAT results in dysregulation of energy metabolism and accumulation of acetyl-CoA in CRAT-mKO hearts (Extended Data Fig. 2c)[4,8]. Acetyl-CoA is a common end product of fatty acid, glucose and amino acid breakdown and serves as a major substrate or allosteric modulator of numerous pathways. To identify the mechanisms underlying CRAT deficiency-induced mtDNA stress, we further analyzed our RNA-seq data and found that there were 700 genes upregulated and 805 genes downregulated (Extended Data Fig. 7a,b). Notably, gene set enrichment analysis (GSEA) indicated that pathways involved in cholesterol homeostasis were among those most affected in CRAT-deficient NRVMs (Extended Data Fig. 7c,d). Specifically, the expression of genes involved in the bile acid synthesis pathway affecting cholesterol catabolism was dramatically increased (Fig. 4a-c). In contrast, the expression of genes involved in cholesterol biosynthesis was significantly decreased (Extended Data Fig. 7e). As acetyl-CoA is the sole carbon building block in mevalonate synthesis, we hypothesized that the increased acetyl-CoA level induced by CRAT depletion may lead to augmentation of intracellular cholesterol level, which in turn triggers feedback responses to promote cholesterol catabolism and suppress cholesterol biosynthesis[16]. Indeed, we found that cholesterol levels were significantly increased in both CRAT-deficient NRVMs and adult CMs isolated from CRAT-mKO mice (Fig. 4d,e).

Bile acid synthesis can be initiated by either cholesterol 7α-hydroxylase (CYP7A1) of the classic pathway in liver or by mitochondrial sterol 27-hydroxylase (CYP27A1) of the acidic pathway in various tissues[17]. We confirmed that the expression of major enzymes involved in the acidic pathway, including CYP27A1, CYP7B1 and HSD3B7, was substantially increased in CRAT-deficient NRVMs (Fig. 4c). Notably, we observed increased accumulation of 7α-hydroxyl-3-oxo-4-cholestenoic acid (7-HOCA), a key intermediate of the acidic pathway[18], and muricholic acid (MCA) but not chenodeoxycholic acid (CDCA; Fig. 4f), suggesting that CDCA may be rapidly converted to MCA in NRVMs[19]. It has been suggested that hydrophobic bile acids such as CDCA are cytotoxic and can cause DNA damage and induce the opening of mPTP in a dose-dependent manner[20,21]. Thus, we hypothesized that bile acids or intermediates of bile acid synthesis might promote mtDNA release into cytosol and trigger type I interferon responses in CMs. To test this hypothesis, we treated NRVMs with CDCA and observed a dose-dependent increase in ISG expression (Extended Data Fig. 8a,b). As MCA is converted from CDCA by hydroxylation at the C-6 position, MCA is more hydrophilic and less cytotoxic than CDCA[22]. In contrast, 7-HOCA is expected to be more hydrophobic than CDCA based on its chemical structure (Fig. 4a), suggesting that it may be more cytotoxic to CMs than CDCA. As expected, we demonstrated that NRVMs were more sensitive to 7-HOCA than CDCA (Extended Data Fig. 8c). 7-HOCA promoted the release of mtDNA into cytosol and triggered a marked induction

in ISG in NRVMs (Fig. 4g,h and Extended Data Fig. 8c). In contrast, MCA was not able to induce ISG expression even at high concentrations (Extended Data Fig. 8d).

To ensure that the increased accumulation of bile acids or intermediates was responsible for the type I interferon responses induced by CRAT depletion, we treated CRAT-deficient NRVMs with GW9662, an antagonist of peroxisome proliferator activated receptors, which play key roles in the transcriptional regulation of *Cyp27a1* in human monocytes[23]. As expected, GW9662 blocked the increase in *Cyp27a1* expression induced by CRAT deficiency (Extended Data Fig. 9a). Notably, *Cypb1* expression was also dramatically inhibited by GW9662 (Extended Data Fig. 9b), suggesting a potential role of PPARs in regulating *Cypb1* expression. More notably, we demonstrated that GW9662 largely abrogated ISG induction in CRAT-deficient NRVMs (Extended Data Fig. 9c). Although GW9662 is considered as a selective PPARγ antagonist, GW9662 inhibits both PPARγ and PPARα with half-maximum inhibitory concentration (IC_{50}) values of 3.3 nM and 32 nM, respectively[24]. A more potent and selective PPARγ antagonist, T0070907, was not able to inhibit ISG expression in CRAT-deficient NRVMs (Extended Data Fig. 9d), suggesting that PPARα may be responsible for the increased expression of ISGs induced by CRAT deficiency. To verify this hypothesis, we knocked down the expression of PPARα in NRVMs and confirmed that loss of PPARα largely inhibited the type I interferon responses in CRAT-deficient NRVMs (Fig. 4i-l).

To investigate the roles of CRAT in bile acid synthesis and type I interferon responses in vivo, we isolated adult CMs from CRAT-WT or CRAT-mKO mice. Metabolomics analysis confirmed that knockout of CRAT led to the intracellular accumulation of 7-HOCA but not MCA in adult CMs isolated from CRAT-mKO mice (Fig. 4m,n). ISG expression was also significantly increased in adult CMs isolated from CRAT-mKO mice (Fig. 4o-r). Finally, we sought to deplete PPARα in vivo by injecting mice with AAV9-sh-*Pparα* virus and demonstrated that knockdown of PPARα abrogated the increase in 7-HOCA level and ISG expression in adult CMs isolated from CRAT-mKO mice (Fig. 4m-r). Taken together, these results reveal a notable role of CRAT in cholesterol homeostasis in CMs. Loss of CRAT leads to increased expression of bile acid synthesis enzymes such as CYP27A1 and results in intracellular accumulation of 7-HOCA, which in turn induces mtDNA stress and triggers the type I interferon responses.

Depletion of CRAT activates a DNA-sensing AIM2 inflammasome

Recognition of microbial DNA or aberrant self-DNA plays a key role in initiating the innate immune response in mammalian cells. Cytosolic double-stranded DNA can also trigger the activation of a DNA-sensing AIM2 inflammasome, an innate immune complex that promotes pro-inflammatory caspase-1 cleavage and activation[25]. Under basal conditions, AIM2 is mostly detected in the small intestine and selective hematopoietic cell types[26]; however, its expression can be rapidly induced by type I interferons[27], suggesting that AIM2 inflammasome activation is dependent on or can be amplified by the type I interferon responses. Indeed, we found that AIM2 was barely detectable in NRVMs at steady state; however, its expression was substantially increased in CRAT-deficient NRVMs (Fig. 3c,f). Thus, we sought to determine whether the AIM2 inflammasome could be activated in

CRAT-deficient NRVMs. We first performed immunofluorescence microscopy to detect the endogenous AIM2, which demonstrated diffuse, weak staining in NRVMs (Fig. 5a). Of note, knockdown of CRAT induced widespread formation of AIM2-positive specks (Fig. 5a), a classic indicator of inflammasome assembly[28].

To examine whether mtDNA fragments can activate the AIM2 inflammasome, we first performed an in vitro caspase-1 activation assay with purified recombinant AIM2 and ASC. Incubation of recombinant AIM2 and ASC with either mtDNA or poly (dA:dT) led to pro-caspase-1 cleavage, suggesting that mtDNA can activate the AIM2 inflammasome in vitro (Extended Data Fig. 10). Inflammasome activation was then confirmed by the cleavage and activation of pro-caspase-1 in CRAT-deficient NRVMs (Fig. 5b,c). Increased proteolytic maturation and secretion of IL-1β were also evident in CRAT-deficient NRVMs (Fig. 5b,d). Active caspase-1 can promote GSDMD cleavage and induce pyroptosis, a proinflammatory type of cell death[29,30]. As expected, we also observed GSDMD cleavage in CRAT-deficient NRVMs (Fig. 5b). It has been reported that pyroptotic cell death results in cell swelling, actin cytoskeleton destruction and chromosome DNA cleavage[31,32]. Therefore, to further confirm whether loss of CRAT leads to pyroptosis, we performed immunofluorescence for cardiac troponin-T (cTnT) to assess actin cytoskeleton structure in NRVMs. As expected, cTnT existed in a very organized pattern along the myofibrils in wild-type (WT) NRVMs (Fig. 5e). In contrast, we observed dramatic changes in morphology with largely disrupted sarcomere organization and diffuse distribution of cTnT in NRVMs transduced with lentivirus expressing *Crat* shRNA (Fig. 5e). Furthermore, we demonstrated that knockdown of CRAT significantly increased the number of TUNEL-positive NRVMs (Fig. 5f), indicating that depletion of CRAT eventually leads to pyroptosis[33]. Finally, depletion of AIM2 substantially inhibited the cleavage of pro-caspase-1 and GSDMD induced by knockdown of CRAT (Fig. 5g-i), indicating that AIM2 was required for inflammasome activation in CRAT-deficient NRVMs. Collectively, these data demonstrate that mtDNA stress induced by CRAT deficiency activates AIM2 inflammasome in NRVMs.

Depletion of casp1, AIM2 or cGAS alleviates cardiac damage

Elevated circulating levels of proinflammatory cytokines, such as IL-1β, IL-6 and TNF-α, are associated with HF severity and prognosis[34-36]. Although clinical trials to block TNF-α failed to improve the outcomes in patients with HF[37,38], a recent prespecified analysis of the CANTOS (canakinumab anti-inflammatory thrombosis outcomes study) trial found that IL-1β blockade significantly reduced HF-related hospitalization and mortality[39]. Further, knockout of IL-1 receptor improves cardiac function and fibrotic remodeling after myocardial infarction[40,41]. These preclinical and clinical studies suggest that IL-1β plays a causal role, rather than serving as a marker of ongoing inflammation in HF. In addition, GSDMD-mediated CM pyroptosis is also evident in patients with DCM and negatively correlated with cardiac contractile function[42]. As both IL-1β and GSDMD require caspase-1 for their maturation and activation, we decided to ablate caspase-1 in CRAT-mKO mice to determine whether inflammasome activation is responsible for the impaired cardiac function observed in CRAT-mKO mice. As expected, we demonstrated that IL-1β levels in both serum and heart tissues were significantly increased in CRAT-mKO mice and that combined deletion of caspase-1 largely abrogated the increases (Fig. 6a,b). Consistent with

these observations, macrophage recruitment in the myocardium was significantly decreased in CRAT and caspase-1 double-knockout mice (CASP1/CRAT-KO) (Fig. 6c,d). Finally, deletion of caspase-1 reversed the increase in HW:TL ratio induced by CRAT deficiency (Fig. 6e). Echocardiographic analysis demonstrated that cardiac contractile function was also significantly improved when caspase-1 was deleted in CRAT-mKO mice (Fig. 6f,g). Notably, we still observed mild but significant decreases in ejection fraction and fractional shortening in CASP1/CRAT-KO mice compared to control mice (Fig. 6f,g), suggesting that chronic activation of the type I interferon pathway in CMs may also be an additional contributing factor of HF.

To verify the role of cGAS and AIM2 in inflammasome activation and impaired cardiac function induced by knockout of CRAT, we sought to knock down the expression of cGAS or AIM2 in adult CMs with AAV9-sh-*cGas* or AAV9-sh-*Aim2* virus in CRAT-mKO mice. Echocardiographic analyses indicated that knockdown of either cGAS or AIM2 significantly improved cardiac contractile function in CRAT-mKO mice (Fig. 6h). As expected, we demonstrated that AIM2 expression was markedly increased in adult CMs isolated from CRAT-mKO hearts and the increase was completely abolished by silencing *cGas* or *Aim2* (Fig. 6i). More notably, we confirmed that inflammasome was activated in adult CMs isolated from CRAT-mKO hearts, as shown by the cleavage of pro-caspase-1 and GSDMD, which was largely inhibited by knockdown of cGAS or AIM2 (Fig. 6i,j). Taken together, our data demonstrate that depletion of CRAT in adult CMs also leads to cGAS-dependent AIM2 inflammasome activation in vivo, which contributes to myocardial inflammation and impaired cardiac function observed in CRAT-mKO mice.

Discussion

In summary, our observations identify an unappreciated role of CRAT in cholesterol metabolism and cell-intrinsic innate immune responses, which contribute to chronic myocardial inflammation and HF progression (Fig. 7). Mounting evidence indicates that chronic inflammation plays a crucial role in the pathogenesis and progression of HF. Proinflammatory cytokines have been shown to directly induce cardiac dysfunction and promote adverse cardiac remodeling[43-45]; however, the relationship between inflammation and HF is complex and bidirectional. Myocardial injury or virus infection often leads to acute activation of innate and adaptive immune systems in the heart. Crosstalk between the heart and other peripheral tissues may also contribute to myocardial inflammation[46]. The mostly neutral results of anti-cytokine or anti-inflammatory therapies for patients with HF reflect our lack of understanding of the precise biology of chronic inflammation in failing hearts. Unfortunately, much of our knowledge about the role of inflammation in the progression of HF has originated from studies of acute myocardial injury, which is quite different from chronic myocardial inflammation[2]. Increased infiltration and activation of inflammatory cells have been observed in the hearts of patients with HF without any discernible myocardial injury or viral infection[47]. Here, we show that dysregulation of cholesterol metabolism induced by deletion of CRAT directly triggers type I interferon responses and promotes the DNA-sensing AIM2 inflammasome activation in CMs, which is sufficient to induce DCM. Our data reveal a potential role of the CM-intrinsic type I interferon responses and AIM2 inflammasome activation by sensing mtDNA stress in the

pathogenesis of HF, implicating that therapeutic effect of anti-cytokine strategies may be limited by the nature of chronic myocardial inflammation under certain pathophysiological conditions. Recently the CANTOS trial showed encouraging effects of IL-1β blockade to reduce HF-related hospitalization and mortality. Our observations that deletion of caspase-1 blocks the increase in serum IL-1β level and significantly improves cardiac contractile function in CRAT-mKO mice provide an explanation for these human studies; however, caspase-1-dependent CM pyroptosis also contributes to myocardial dysfunction[42], which theoretically cannot be alleviated by anti-IL-1β therapy. In addition, sustained activation of type I interferon responses may also contribute to the progression of HF[48]. Although we have demonstrated that depletion of cGAS inhibits type I interferon responses and AIM2 inflammasome activation induced by CRAT deficiency, we have no direct evidence supporting that type I interferon responses contribute to DCM progression. Future studies with cell-specific interferon-α/interferon-β receptor knockout mice will provide more insights. Nevertheless, more detailed characterization of inflammatory phenotype in patients with HF is needed for designing efficient anti-inflammatory therapies.

CRAT plays a central role in regulating metabolic flexibility by catalyzing the conversion of acetyl-CoA to acetylcarnitine, which enables its mitochondrial export into cytosol[4]. Our data reveal an unexpected role of CRAT in cholesterol catabolism. Loss of CRAT activity disrupts energy metabolism and leads to an increase in acetyl-CoA level (Extended Data Fig. 2c)[4,8]. Because acetyl-CoA is the only carbon building block of cholesterol biosynthesis, we propose that increased acetyl-CoA levels may initially promote cholesterol synthesis, which is then counterbalanced by increased cholesterol clearance through bile acid synthesis pathway to maintain cholesterol homeostasis in CMs. There are about 17 different enzymes involved in the bile acid synthesis pathway and only the liver has a complete set of them[17]. Thus, most of the oxidized intermediates such as 7-HOCA in the peripheral tissues must be transported to the liver for their final conversion to bile acids[19]. We expect that substantially increased expression of CYP27A1, CYP7B1 and HSD3B7 eventually leads to the accumulation of 7-HOCA in CRAT-deficient cells, which induces mtDNA stress and triggers innate immune responses. It is worth noting that we also observe a significant increase in MCA levels in CRAT-deficient NRVMs (Fig. 4f), indicating that CMs can convert cholesterol to bile acids even when some of the critical enzymes such as AKR1D1or AKR1C4 are not detected in these cells (Fig. 4b). Possible explanations include that their expression levels are very low or that other alternative enzymes may fulfill their functions in NRVMs. Finally, it is well documented that hyperlipidemia and chronic inflammation are closely interrelated[49]. For example, crystalline cholesterol acts as a damage-associated molecular pattern and induces NLRP3 inflammasome activation in lipopolysaccharide (LPS)-primed human phagocytes[50]. It remains largely unknown whether CMs can ingest or accumulate cholesterol crystal. Regardless, our current findings raise an intriguing hypothesis that elevated low-density lipoprotein cholesterol may increase intracellular cholesterol level and promote chronic inflammation associated with the loss of CRAT activity, which has been observed in pathophysiological conditions such as pressure overload, diabetes and obesity[5,51].

Methods

Reagents and antibodies

All the chemicals and antibodies are listed in the main reagent table (Supplementary Table 1).

Mice

CRAT-mKO mice were generated through the breeding of *Crat* (flox/flox)[4] and Myh6-MerCreMer mice following tamoxifen injection. CRAT and caspase-1 double-knockout mice (CASP1/CRAT-KO) were generated through the breeding of CRAT-mKO and CASP1 KO mice. All mice were housed in a controlled environment with a 12-h light–dark cycle, room temperature of 21–23 °C, humidity at 45–65% and food and water ad libitum. Both male and female mice aged 2–4 months were used for the experiments. No significant sex differences were observed, so the data for male and female mice were combined and presented together. All experimental procedures on mice were performed according to the National Institutes of Health Guide for the Care and Use of Laboratory Animals and approved by the Institutional Committee for the Use of Animals in Research at Baylor College of Medicine.

Cell culture and lentiviral transduction

Primary NRVMs were isolated from 1–2-day-old Sprague–Dawley rat pups following our established methods[52]. The Worthington neonatal CM isolation system kit was used following the manufacturer instructions. NRVMs were maintained in MEM, supplemented with 10% horse serum, 5% fetal bovine serum (FBS) and antibiotics (100 U ml^{-1} penicillin, 68.6 mmol ml^{-1} streptomycin). Two days after plating, NRVMs were transduced with lentiviral as needed. Cells were then treated with indicated chemical reagents.

Generation of lentiviral particles

Lentiviral vectors encoding *Crat*, *cGas*, *Ppara*, *Aim2* shRNAs or control vectors were obtained from Origene. HEK293 cells were grown in DMEM supplemented with 10% FBS and antibiotics (100 U ml^{-1} penicillin and 68.6 mol l^{-1} streptomycin). These lentiviral plasmids were co-transfected with lentiviral packaging plasmids psPAX2 and pMD2.G in HEK293T cells to ensure lentiviral particles production following our published protocol[52].

Immunoblotting, immunohistochemistry and immunofluorescence

Immunoblotting was performed based on our established method[52]. Briefly, cells or homogenized tissues were lysed with the lysis buffer (1% Triton X-100, 50 mM Tris, pH 7.4, 150 mM NaCl, 10% glycerol and protease and phosphatase inhibitors) and clarified by centrifugation at 14,000*g* for 10 min. Equal amounts of protein were separated by SDS–PAGE gel and western blots were then performed with the indicated antibodies (1:1,000 dilution). Tissues for immunohistochemistry were collected following terminal euthanasia of the mice according to our established methods[52]. Mice were perfused with PBS and then with 4% paraformaldehyde from transversal aorta, followed by either paraffin-embedded or frozen sectioning. For frozen sectioning, the fixed hearts were incubated with

15% sucrose, 30% sucrose gradient and then embedded in Tissue-Tek Cryomold (Sakura, Electron Microscopy Sciences) containing Optimal Cutting Temperature compound (Fisher Scientific). Paraffin-embedded sections were prepared at an average thickness of 5–7 μm for eosin hematoxylin or Masson's trichrome staining. Frozen sections or cultured cells were subjected for immunostaining with the indicated antibodies (1:100 dilution) following our previous publications[53].

Gene expression analysis (real-time PCR and RNA-seq)

Total RNAs were reverse transcribed into complementary DNAs with an iScript cDNA synthesis kit. The specific pairs of primers used for real-time PCR are listed in Supplementary Table 2 (designed by Universal ProbeLibrary Assay Design Center tool from Roche). Real-time PCR was performed with FastStart Universal Probe Master mix, specific primers and probes for each gene in Roche Lightcycler 480 PCR machine. Reaction mixtures were incubated at 95 °C for 10 min followed by 55 cycles at 95 °C for 10 s and 60 °C for 30 s. Housekeeping genes were 18s and β-actin. Total RNAs isolated from NRVMs were processed to generate cDNA libraries that were sequenced on the Illumina HiSeq 2500 platform by the Baylor RNA Profiling Core laboratories. We used Kallisto to map RNA-seq reads to the rat (*Rattus norvegicus*) reference genome mRatBN7.2 and quantified transcript abundance[54]. The rat reference gene set was downloaded from the Ensembl database (release-105; http://ftp.ensembl.org/pub/release-105/gff3/rattus_norvegicus/). Kallisto (v.0.46.0) uses a bootstrapping technique to estimate transcript abundance and its uncertainties by resampling the sequence reads. In this study, we applied this bootstrapping technique to repeat the analysis 100 times. We used DESeq2 v.1.20, a R package for differentially expressed gene (DEG) analysis, to estimate the significance of differential expression and calculate *P* values from transcript abundance data[55]. We then used the Benjamini–Hochberg method to adjust *P* values and define DEGs using adjusted *P* values of no more than 0.05 as the criterion. For the hallmark analysis, we downloaded hallmark gene sets from MSigDB (https://www.gsea-msigdb.org/gsea/msigdb/index.jsp) and applied GSEA to assess the significance of associations between DEGs and hallmark genes[56].

Single-cell RNA-sequencing analysis

Gene expressions were obtained from the original publication under GEO accession numbers GSE109816 and GSE121893 (ref. 6). The scRNA-seq data analysis was performed using SCANPY package v.1.8.2 (ref. 57). Specifically, scRNA-seq data were normalized using 'scanpy.pp.normalize_total' function. The top 2,000 highly variable genes were detected by 'scanpy.pp.highly_variable_gene' function. The expression of genes was further normalized with 'sc.pp.log1p'. The *t*-SNE analysis was performed by 'scanpy.tl.tsne' function with the principal components calculated by 'scanpy.tl.pca'. We obtained cell types in this dataset from the original publication. The significance of the differential expression of CRAT between healthy and HF samples was measured with a one-sided Wilcoxon rank-sum test by the SciPy Python package v.1.7.2 (ref. 58).

CRAT enzymatic activity assay

CRAT enzymatic activity was measured in 250 μl reaction buffer with 50 μg of crude mitochondrial suspension in 96-well microplate by using a Tecan Ultraspec 3000 spectrophotometer. The reaction buffer contains 20 mM HEPES, 1 mM EGTA, 220 mM sucrose, 40 mM KCl, 0.1 mM 5,5′-dithio-bis (2-nitrobenzoic acid) (Sigma), 1.3 mg ml^{-1} free-FA BSA (Roche Diagnostics) and 40 μM acetyl-CoA (Sigma). Densitometry was read once at 420 nm and then initiated by adding L-carnitine (Sigma) at 1 mM simultaneously in each well. Optical density was monitored for 4 min following the addition of L-carnitine.

Analysis of endocrine hormones and metabolites

Serum and heart lysates were subjected for inflammatory cytokine measurements with their ELISA kits following the manufacturer's protocols. Cholesterol contents in the heart were measured with Infinity total cholesterol kits. Acetyl-CoA levels in the heart were measured with kits following the manufacture's protocol.

Bile acid analysis

Bile acids were extracted from cells using the liquid-liquid extraction method and analyzed through high-throughput liquid chromatography–mass spectrometry (LC–MS/MS) described previously[59,60]. The pooled sample was used as quality control. The extracted bile acids were separated through the ACQUITY UPLC BEH C18, 1.7 μm (2.1 × 100 mm) HPLC column with 45 °C of column temperature. The mobile phases A and B were water:methanol (80:20) in 10 mM ammonium acetate (A) and acetonitrile:water (90:10) in 10 mM ammonium acetate (B). Gradient flows were 0–0.5 min 5% B, 0.5–12 min 98% B, 12–13 min 98% B and 13 min 5% B, followed by re-equilibration until the end of the gradient, 15 min from the initial starting condition of 5% B. The flow rate of the solvents used for analysis was 0.2 ml min^{-1} and the injection volume was 20 μl. MS data were acquired in the negative ionization mode via multiple reaction monitoring using a 6495 Triple Quadrupole MS coupled to an HPLC system (Agilent Technologies) and operated by Agilent Mass Hunter Software (v.11.0)[59,60]. The peak integration and data analysis were performed using Agilent Mass Hunter Quantitative Analysis software.

Echocardiography

Transthoracic echocardiography was performed following our established method[52]. Briefly, mice were anesthetized with 2% isoflurane and restrained on a temperature-controlled mouse board. Echocardiography was then performed by using Vevo F2 (Visual Sonics). An echocardiographer blind to animal genotypes captured two-dimensional parasternal long-axis and short-axis views at the level of the papillary muscles of the left ventricle. The heart rate was recorded and various parameters including EF, FS and LVID at end diastole and LVID at end systole were calculated by Vevo Lab v.3.2.0 software.

Detection of mtDNA in cytosolic extracts

Mitochondrial and cytosol fractionation was performed following our established protocol[52]. Briefly, cells were centrifuged at 700*g* for 10 min at 4 °C. Cell pellets were suspended in mitochondrial reagent A with protease inhibitors, vortexed for 2 min and then mixed with 10

μl mitochondrial reagent B. After 5 min of incubation on ice, 400 μl mitochondrial Isolation regent C was added and the tubes were centrifuged at 700*g* for 10 min at 4 °C. The collected supernatant was then re-centrifuged at 12,000*g* for 15 min at 4 °C. The supernatant was cytosol fractions and mitochondrial pellet was re-suspended in BSA-free MIB containing 10 mM KH_2PO_4 and 5 mM $MgCl_2$ (pH 7.2). The mitochondrial DNA was extracted using a QIAamp DNA Mini kit. The cytosol DNA was prepared by performing phenol–chloroform isoamyl alcohol extraction methods. The cytosol DNA mixture and mitochondrial DNA mixture were subjected to quantitative PCR assays for mtDNA using its specific primers (D-loop1-3; Supplementary Table 2).

In vitro caspase-1 purification and activation assays

pET21b-his-caspase-1 plasmid was transformed to BL21(DE3) competent cells. After IPTG induction for 5 h, cells were collected and his-caspase-1 protein was purified by using HisPur Cobalt Resin (Thermo Scientific) basing on its own protocol. To remove excess imidazole, we dialyzed the protein with PBS. Purified His-caspase-1 (2 μg) was then incubated with recombinant GST–AIM2 (2 μg) and ASC protein (1 μg) in the presence or absence of mtDNA or poly (dA:dT) (1 μg) (InvivoGen) in TE buffer for 30 min at 37 °C. mtDNA was amplified by PCR using primers for D-loop1 and 2 (Supplementary Table 2). The reaction mixtures were then loaded on SDS-PAGE gel and detected with caspase-1 antibody.

Cardiomyocyte extraction by using Langendorff apparatus

Adult mouse CMs were extracted based on previous published protocols with modifications[61]. Briefly, mice were anesthetized (inhalation of 2% isoflurane in 100% O_2, 1.01 min^{-1}) and then killed by cervical dislocation. The heart was excised and perfused via the aorta with a Tyrode's solution on a Langendorff apparatus with constant flow perfusion by pumping the perfusate, around total of 15 ml perfusion buffer pumped through the heart. The heart was then digested with Tyrode's solution containing Liberase TH (25 mg ml^{-1}; Roche). The ventricles were excised and cut to small pieces in KB buffer. The tissue then was filtrated through a 200-μm micromesh to remove large debris and pellet CMs were collected by centrifugation at 800 r.p.m. at room temperature for 2 min.

Statistics and reproducibility

All experiments were repeated at least three times independently with sufficient sample sizes. All data were analyzed using GraphPad Prism software (v.9) and presented as mean ± s.e.m. or box plots as indicated in the figure legends. Differences were analyzed by Student's *t*-test, one-way or two-way ANOVA followed by a post hoc test as indicated. Values of $P \leq 0.05$ were considered statistically significant. Detailed statistical values are provided in the figure panels.

Reporting summary

Further information on research design is available in the Nature Portfolio Reporting Summary linked to this article.

Extended Data

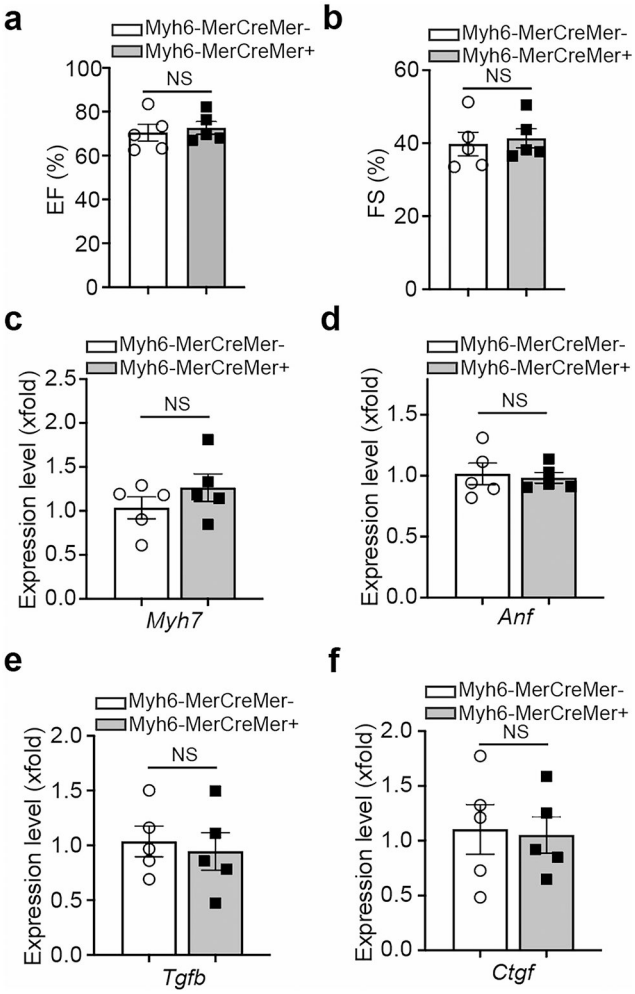

Extended Data Fig. 1 |. Activation of Myh6-MerCreMer with low doses of tamoxifen has no deleterious effects on cardiac function.

Adult Myh6-MerCreMer^{-} or Myh6-MerCreMer + male and female mice were injected with tamoxifen for 4 consecutive days at a dose of 20 mg/kg/day. **a, b**, Echocardiographic analyses were performed to estimate cardiac contractile function after 2 months. **c-f**, RT-PCR analysis of the expression of the hypertrophic marker genes and the pro-fibrotic genes in the hearts. No significant changes were observed between these two groups. n = 5 mice per group. Data are shown as the mean ± SEM. Analysis was unpaired two-tailed Student's *t*-test (**a-f**). NS, not significant.

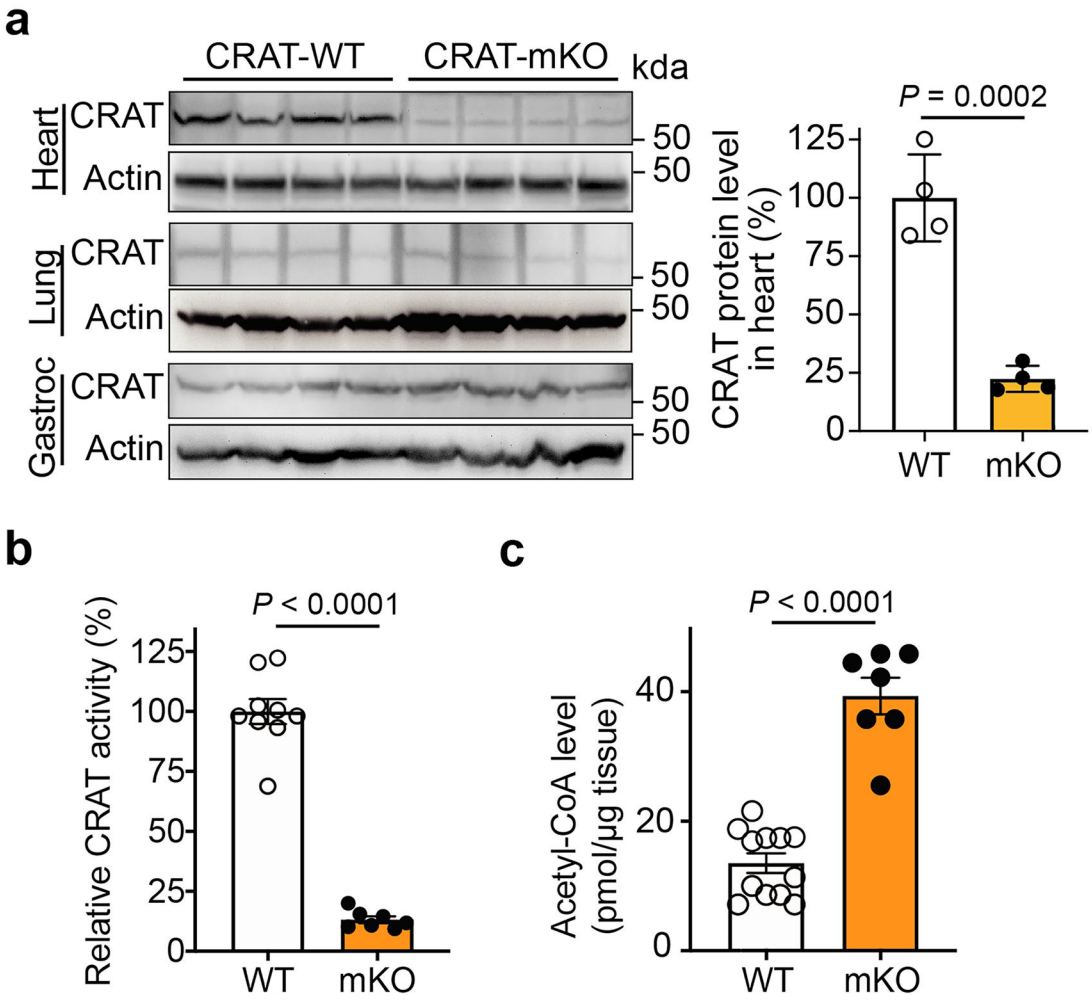

Extended Data Fig. 2 |. Cardiomyocyte-specific deletion of CRAT increases acetyl-CoA level in the hearts.

a, Western-blots showed that CRAT was specifically depleted in CRAT-mKO male and female hearts but not in lungs or gastrocnemius muscles. **b**, CRAT activity was dramatically decreased in CRAT-mKO male and female hearts. **c**, Acetyl-CoA level was significantly increased in CRAT-mKO male and female hearts. n = 4 (**a**), 9 (**b**, WT), 7 (**b**, mKO), 12 (**c**, WT), 7 (**c**, mKO) mice per group. Data are shown as the mean ± SEM. Analysis was unpaired two-tailed Student's *t*-test (**a-c**).

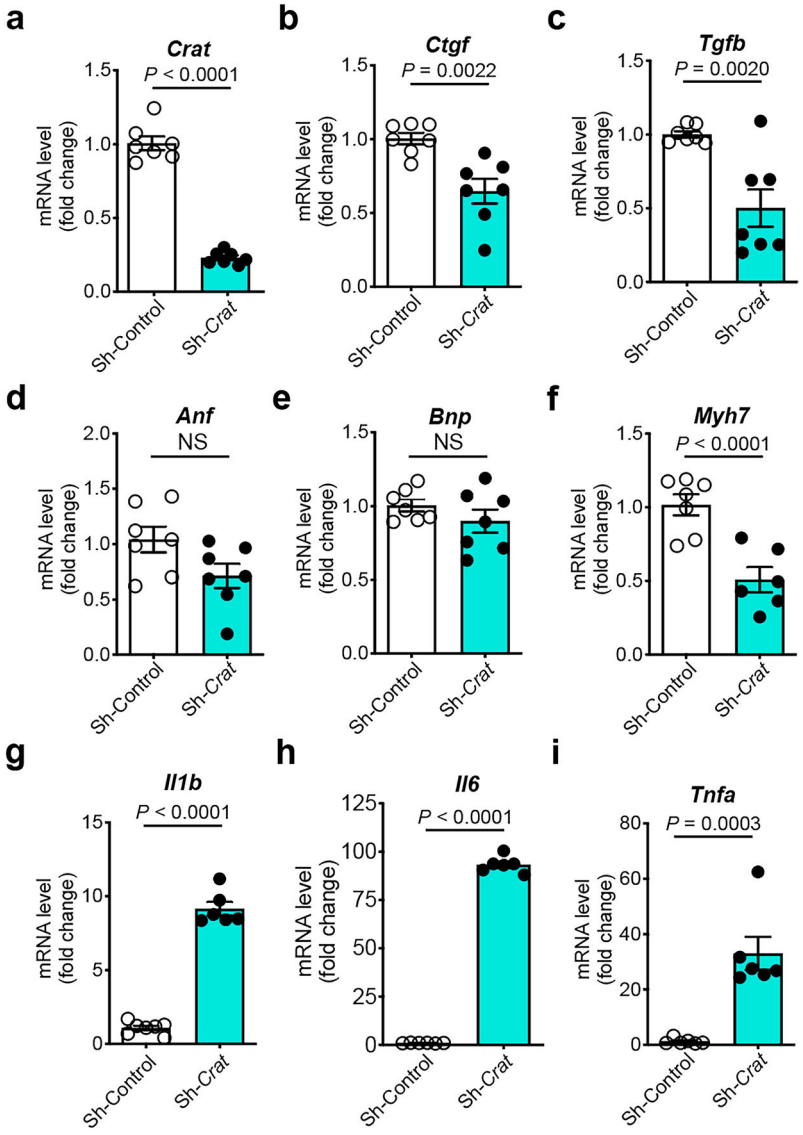

Extended Data Fig. 3 |. Knockdown of CRAT in NRVMs increases the expression of pro-inflammatory cytokines.

NRVMs were transduced with lentivirus expressing *Crat* shRNA or control shRNA for 5 days. RNAs were extracted from the cells and RT-PCRs were then performed to determine the expression of hypertrophy, pro-fibrotic or pro-inflammatory genes. **a**, knockdown of CRAT expression was confirmed by RT-PCR. **b-f**, the expression of hypertrophic and pro-fibrotic genes was not increased by CRAT knockdown. **g-i**, the expression of *Il-1β, Il-6* and *Tnf-α* was substantially increased in CRAT-deficient NRVMs. n = 6-7 (**a-i**, Sh-Control), 6 (**a-i**, Sh-*Crat*) biologically independent samples per group. Data are shown as the mean ± SEM. Analysis was unpaired two-tailed Student's *t*-test (**a-i**). NS, not significant.

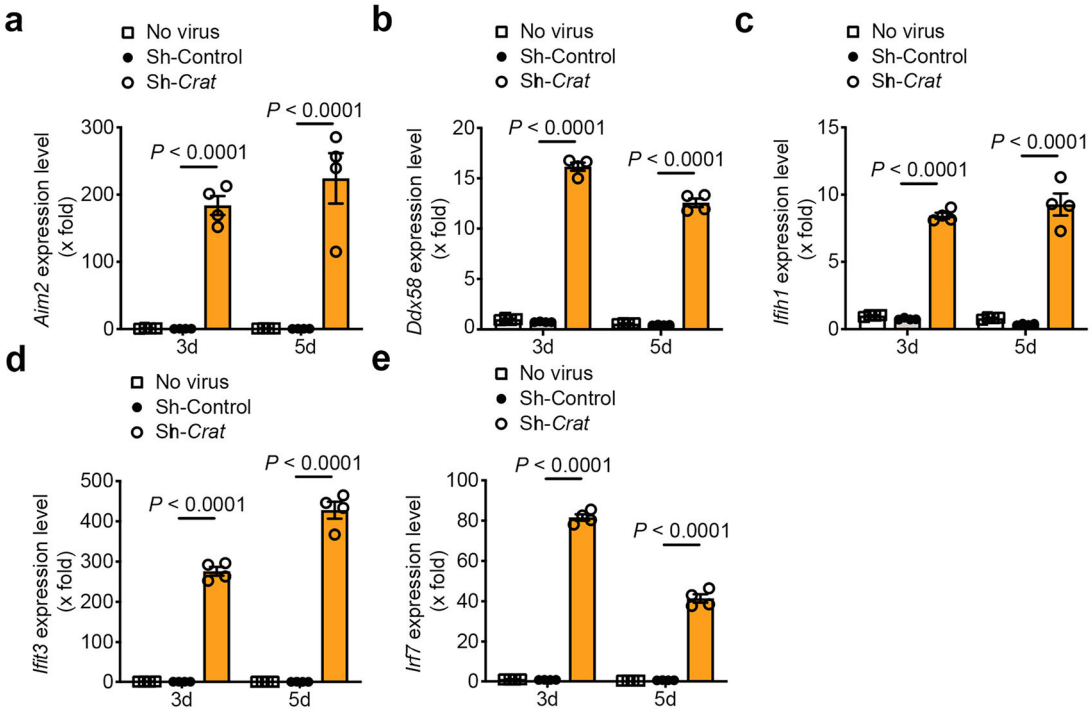

Extended Data Fig. 4 |. CRAT deficiency induces type I interferon responses in NRVMs.
a-e, NRVMs were transduced with lentivirus expressing *Crat* shRNA, control shRNA or no virus for 3 or 5 days. RNAs were extracted from the cells and RT-PCRs were then performed to determine the expression of *Aim2* (a), *Ddx58* (b), *Ifih1*(c), *Ifit3* (d) and *Irf7* (e). n = 4 (**a-e**) biologically independent samples per group. Data are shown as the mean ± SEM. Analysis was two-way ANOVA followed by Bonferroni's multiple comparison test (**a-e**).

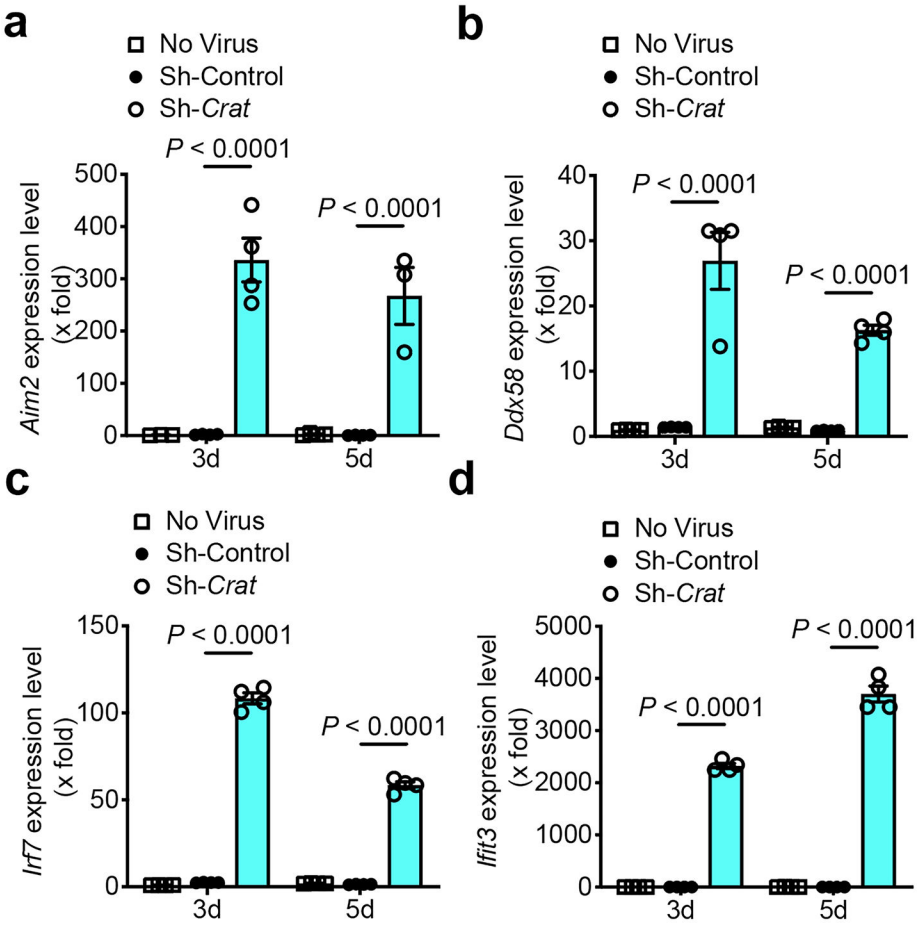

Extended Data Fig. 5 l. CRAT deficiency induces type I interferon responses in cardiac fibroblasts.

a-d, Cardiac fibroblasts were transduced with lentivirus expressing *Crat* shRNA, control shRNA or no virus for 3 or 5 days. RNAs were extracted from the cells and RT-PCRs were then performed to determine the expression of *Aim2* (a), *Ddx58* (b), *Irf7* (c) and *Ifit3* (d). n = 4 (**a-d**, *no virus*, Sh-Control), 3-4 (**a-d**, Sh-*Crat*) biologically independent samples per group. Data are shown as the mean ± SEM. Analysis was two-way ANOVA followed by Bonferroni's multiple comparison test (**a-d**).

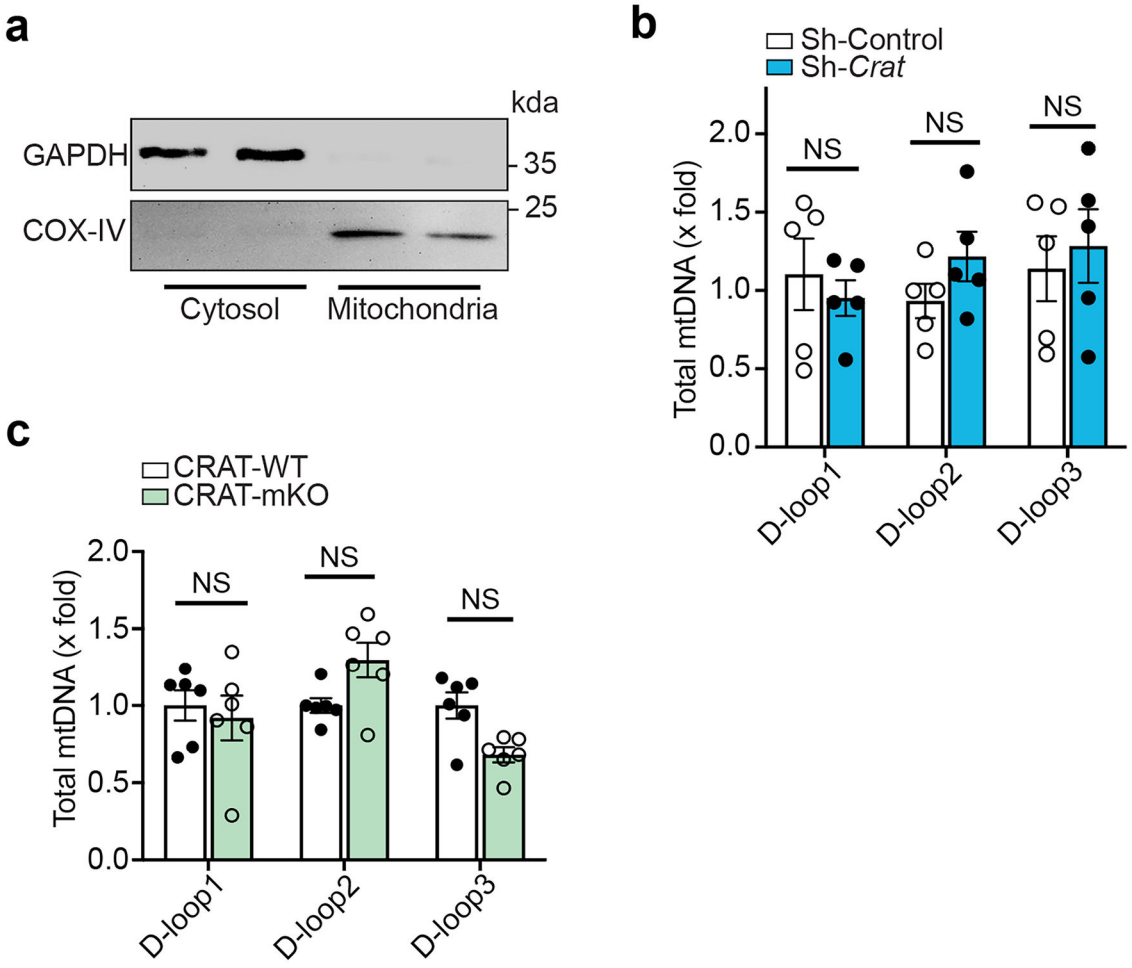

Extended Data Fig. 6 |. Depletion of CRAT has no effect on total mitochondrial DNA level in NRVMs and adult CMs.

a, b, NRVMs were transduced with lentivirus expressing control shRNA or *Crat* shRNA. Cells were harvested and mitochondria and cytosol fractionation was then performed after 5 days. Western blots indicated that there was no contamination between these two fractions (a). RT-PCRs were then performed with mitochondrial fraction to quantify the total mitochondrial DNA level (b). **c**, Adult CRAT-WT and CRAT-mKO male and female mice were injected with tamoxifen (20 mg/kg/day) for four consecutive days. Three weeks later, CMs were isolated from hearts for mitochondria and cytosol fractionation. RT-PCRs were then performed with mitochondrial fraction to quantify the total mitochondria DNA level. n = 5 biologically independent samples (**b**), 6 mice (**c**) per group. Data are shown as the mean ± SEM. Analysis was unpaired two-tailed Student's *t*-test (**b-c**). NS, not significant.

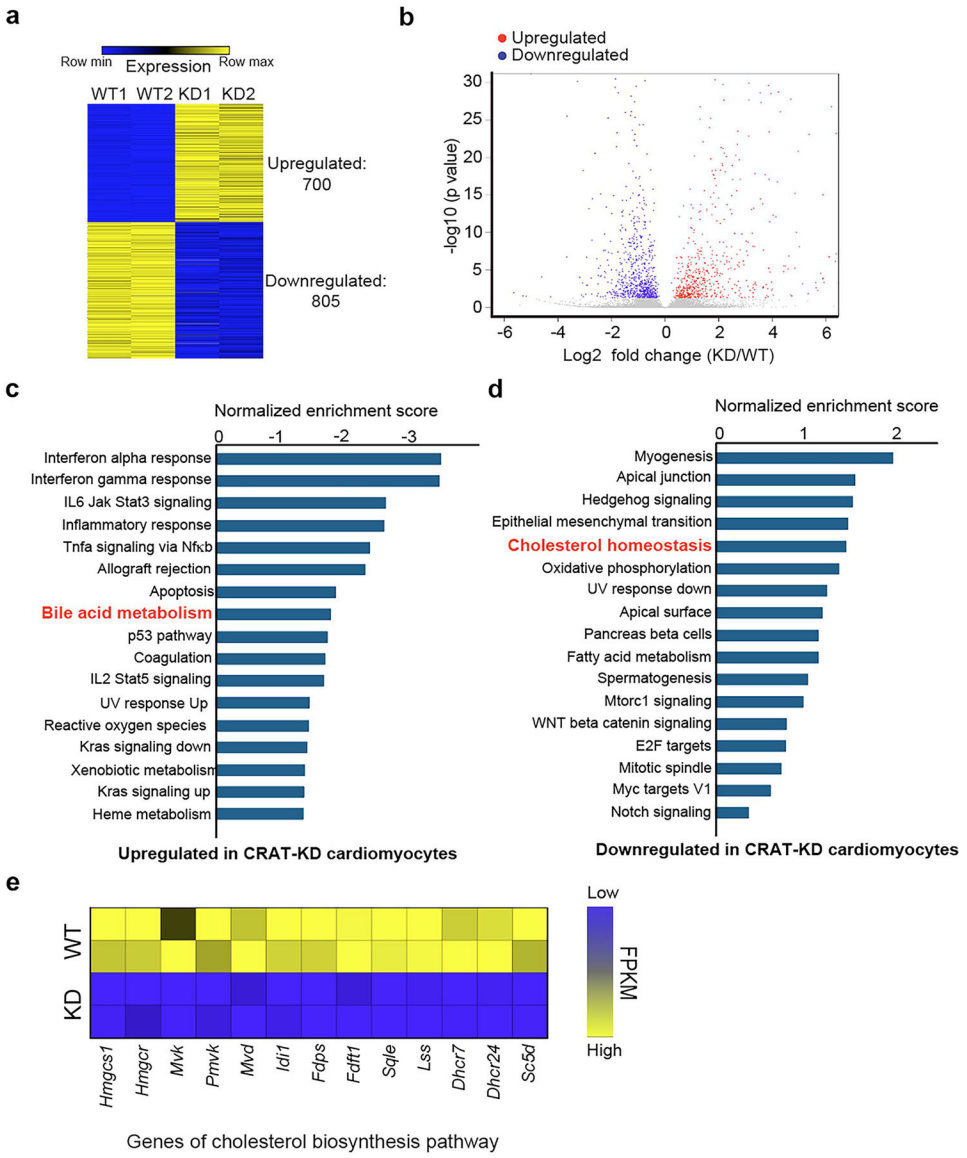

Extended Data Fig. 7 |. RNA-sequencing analysis for NRVMs transduced with lentivirus expressing control shRNA or *Crat* shRNA.

a, b, Heatmap and volcano plot of the significantly differential expressed genes. **c, d**, GSEA analysis of hallmark pathways shows 17 upregulated and 17 downregulated pathways in CRAT knockdown (KD) NRVMs. **e**. Heatmap analysis of the major enzymes involved in cholesterol biosynthesis pathway.

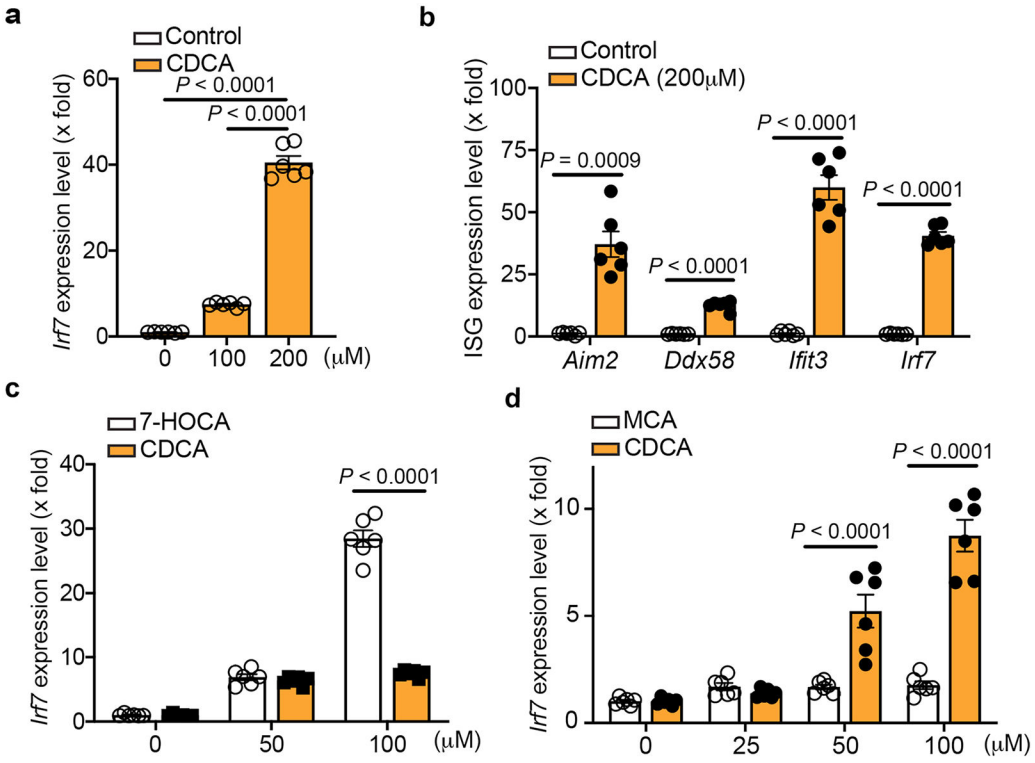

Extended Data Fig. 8 |. Bile acids and 7-HOCA induce type I interferon responses in NRVMs. **a, b**, NRVMs were treated with different doses of CDCA for 1 day. Cells were then harvested for RT-PCR to determine the expression of the indicated ISGs. **c, d**, NRVMs were treated with different doses of CDCA, 7-HOCA or MCA for 1 day. Cells were then harvested for RT-PCR to determine the expression of the indicated ISGs. n = 6 (**a-d**) biologically independent samples per group. Data are shown as the mean ± SEM. Analysis was one-way ANOVA (**a**) or two-way ANOVA (**c-d**) followed by Bonferroni's multiple comparison test and unpaired two-tailed Student's *t*-test (**b**).

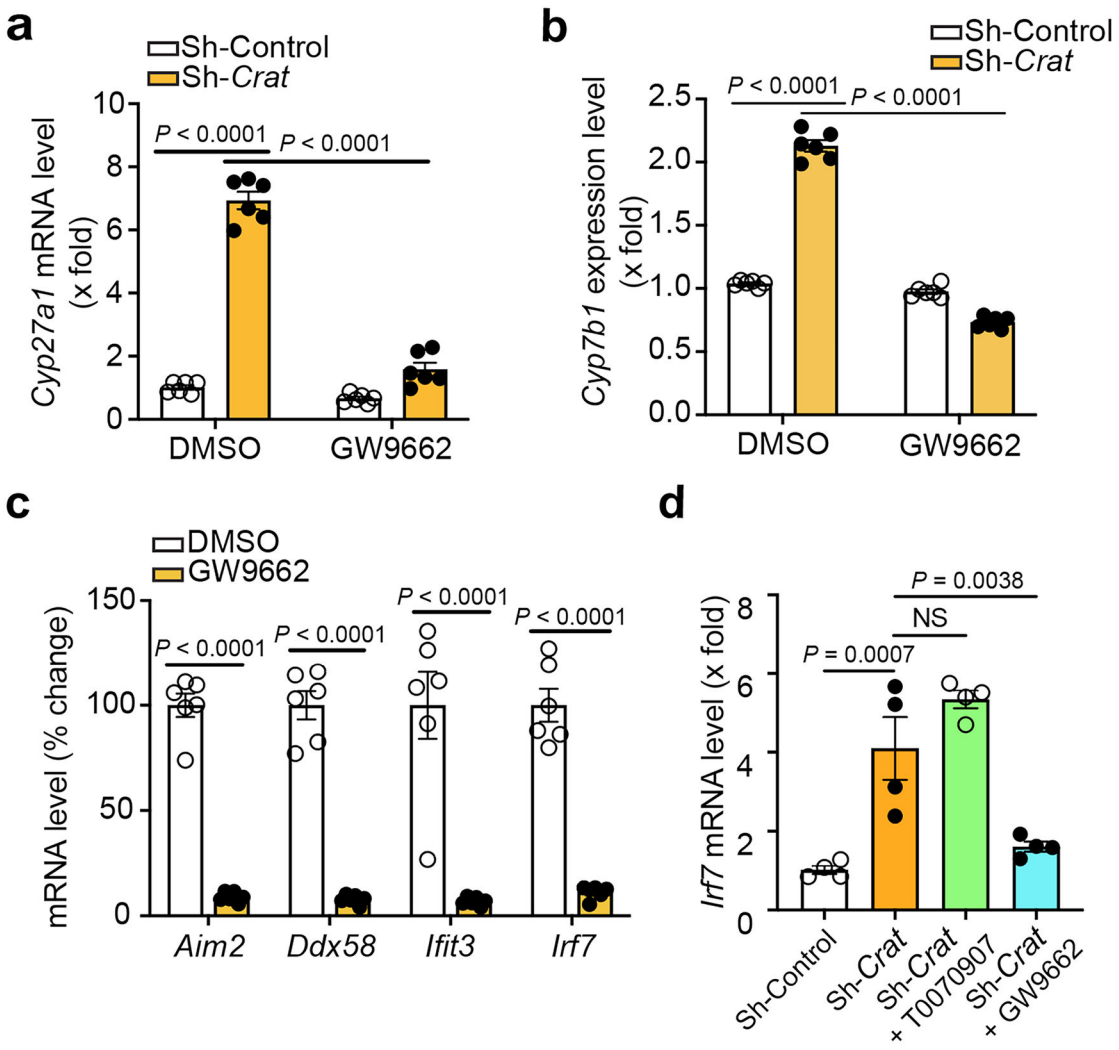

Extended Data Fig. 9 |. PPARs inhibitor, GW9662, inhibits the type I interferon responses in CRAT-deficient NRVMs.

NRVMs were transduced with lentivirus expressing control shRNA or *Crat* shRNA. Cells were then treated with GW9662 (10 μM) or T0070907 (10 μM) as indicated for two days. **a, b**, RT–PCR indicated that GW9662 inhibited the induction of *Cyp27a1* (a) and *Cyp7b1*(b) in CRAT-deficient NRVMs. **c, d**, GW9662 but not T0070907 abolished the increase in ISG expression induced by CRAT depletion. n = 6 (**a-c**), 4 (**d**) biologically independent samples per group. Data are shown as the mean ± SEM. Analysis was two-way ANOVA (**a-b**) or one-way ANOVA (**d**) followed by Bonferroni's multiple comparison test and unpaired two-tailed Student's *t*-test (**c**). NS, not significant.

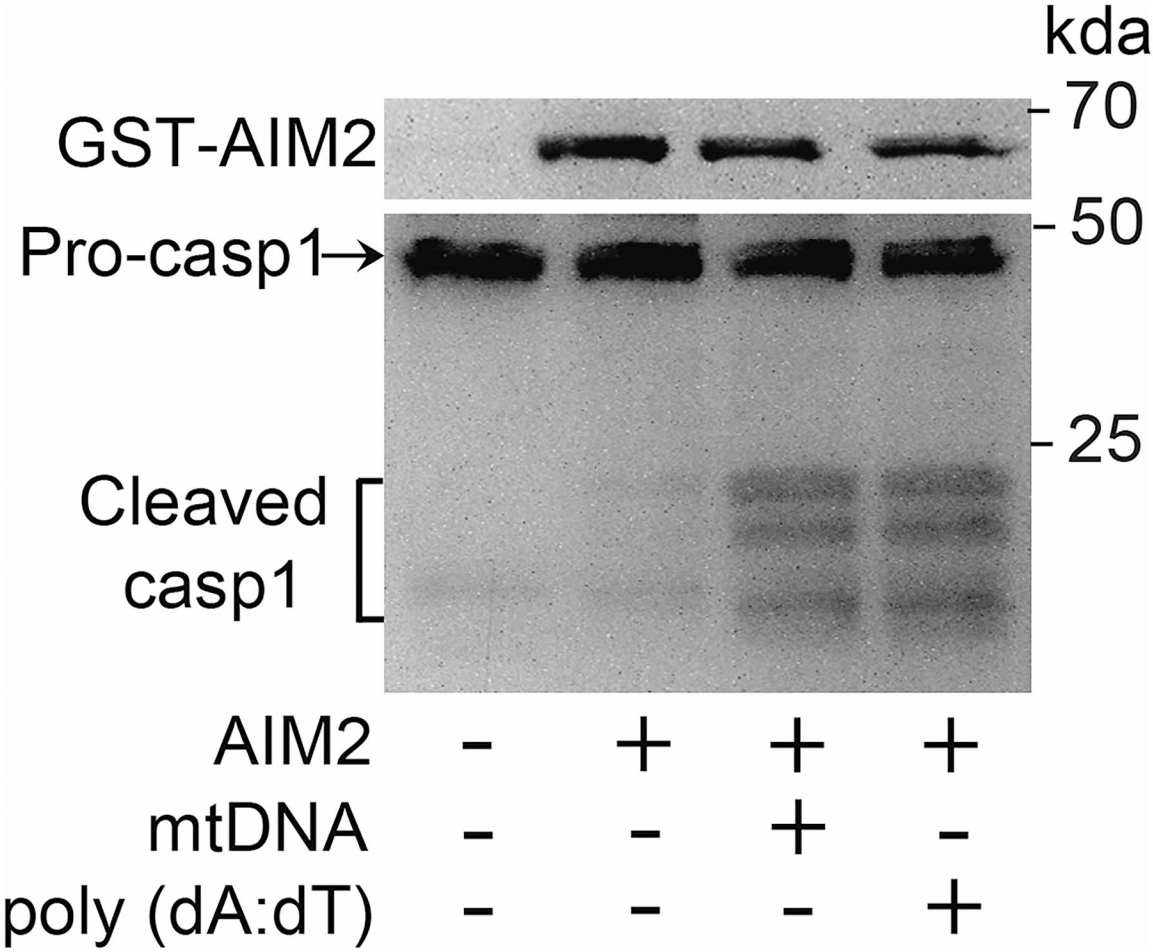

Extended Data Fig. 10 |. Mitochondrial DNA activates AIM2-inflammasome in vitro.
Purified GST–AIM2 (2 μg), ASC protein (1 μg), His-Caspase-1 (2 μg) were incubated in the presence or absence of mtDNA (1 μg) or poly (dA:dT) (1 μg) in TE buffer for 30 min at 37 °C. The reaction mixtures were then loaded on SDS-PAGE gel and Western-blots were performed with the indicated antibodies. Here is the representative result from three independent experiments.

Supplementary Material

Refer to Web version on PubMed Central for supplementary material.

Acknowledgements

This work is supported by National Institutes of Health grants R01 HL122736 (to L.X.), R01 HL166549 (to L.X.) and R01 DK123186 (to X.P.).

Data availability

The data that support the findings of this study are available within the paper in Supplementary Information files. Detailed information of key reagents is provided in Supplementary Table 1. The raw sequence data reported in this paper have been deposited in

GEO (accession no. GSE200057). This RNA-seq dataset, together with the other single-cell RNA-seq datasets GSE109816 and GSE121893 (ref. 6), is publicly accessible at GEO. Source data are provided with this paper.

References

1. Hunt SA et al. ACC/AHA guidelines for the evaluation and management of chronic heart failure in the adult: executive summary a report of the American College of Cardiology/American Heart Association Task Force on practice guidelines (committee to revise the 1995 guidelines for the evaluation and management of heart failure): developed in collaboration with the International Society for Heart and Lung Transplantation; endorsed by the Heart Failure Society of America. Circulation 104, 2996–3007 (2001). [PubMed: 11739319]
2. McDonagh TA et al. 2021 ESC Guidelines for the diagnosis and treatment of acute and chronic heart failure. Eur. Heart J 42, 3599–3726 (2021). [PubMed: 34447992]
3. Doenst T, Nguyen TD & Abel ED Cardiac metabolism in heart failure: implications beyond ATP production. Circ. Res 113, 709–724 (2013). [PubMed: 23989714]
4. Muoio DM et al. Muscle-specific deletion of carnitine acetyltransferase compromises glucose tolerance and metabolic flexibility. Cell Metab. 15, 764–777 (2012). [PubMed: 22560225]
5. Davidson MT et al. Extreme acetylation of the cardiac mitochondrial proteome does not promote heart failure. Circ. Res 127, 1094–1108 (2020). [PubMed: 32660330]
6. Wang L. et al. Single-cell reconstruction of the adult human heart during heart failure and recovery reveals the cellular landscape underlying cardiac function. Nat. Cell Biol 22, 108–119 (2020). [PubMed: 31915373]
7. Bersell K. et al. Moderate and high amounts of tamoxifen in αMHC-MerCreMer mice induce a DNA damage response, leading to heart failure and death. Dis. Model Mech 6, 1459–1469 (2013). [PubMed: 23929941]
8. Davies MN et al. The acetyl group buffering action of carnitine acetyltransferase offsets macronutrient-induced lysine acetylation of mitochondrial proteins. Cell Rep. 14, 243–254 (2016). [PubMed: 26748706]
9. Motwani M, Pesiridis S & Fitzgerald KA DNA sensing by the cGAS–STING pathway in health and disease. Nat. Rev. Genet 20, 657–674 (2019). [PubMed: 31358977]
10. Yu CH et al. TDP-43 triggers mitochondrial DNA release via mPTP to activate cGAS/STING in ALS. Cell 183, 636–649 (2020). [PubMed: 33031745]
11. West AP et al. Mitochondrial DNA stress primes the antiviral innate immune response. Nature 520, 553–557 (2015). [PubMed: 25642965]
12. Kim J. et al. VDAC oligomers form mitochondrial pores to release mtDNA fragments and promote lupus-like disease. Science 366, 1531–1536 (2019). [PubMed: 31857488]
13. Sprenger HG et al. Cellular pyrimidine imbalance triggers mitochondrial DNA-dependent innate immunity. Nat. Metab 3, 636–650 (2021). [PubMed: 33903774]
14. Chapman J, Ng YS & Nicholls TJ The maintenance of mitochondrial DNA integrity and dynamics by mitochondrial membranes. Life 10.3390/life10090164 (2020).
15. Fontana GA & Gahlon HL Mechanisms of replication and repair in mitochondrial DNA deletion formation. Nucleic Acids Res. 48, 11244–11258 (2020). [PubMed: 33021629]
16. Siperstein MD & Fagan VM Feedback control of mevalonate synthesis by dietary cholesterol. J. Biol. Chem 241, 602–609 (1966). [PubMed: 5908125]
17. Russell DW The enzymes, regulation, and genetics of bile acid synthesis. Annu. Rev. Biochem 72, 137–174 (2003). [PubMed: 12543708]
18. Saeed A. et al. 7α-hydroxy-3-oxo-4-cholestenoic acid in cerebrospinal fluid reflects the integrity of the blood-brain barrier. J. Lipid Res 55, 313–318 (2014). [PubMed: 24319290]
19. Chiang JY Regulation of bile acid synthesis: pathways, nuclear receptors, and mechanisms. J. Hepatol 40, 539–551 (2004). [PubMed: 15123373]
20. Botla R, Spivey JR, Aguilar H, Bronk SF & Gores GJ Ursodeoxycholate (UDCA) inhibits the mitochondrial membrane permeability transition induced by glycochenodeoxycholate: a

mechanism of UDCA cytoprotection. J. Pharmacol. Exp. Ther 272, 930–938 (1995). [PubMed: 7853211]

21. Kandell RL & Bernstein C Bile salt/acid induction of DNA damage in bacterial and mammalian cells: implications for colon cancer. Nutr. Cancer 16, 227–238 (1991). [PubMed: 1775385]
22. Guo GL & Chiang JYL Is CYP2C70 the key to new mouse models to understand bile acids in humans? J. Lipid Res 61, 269–271 (2020). [PubMed: 31964761]
23. Quinn CM, Jessup W, Wong J, Kritharides L & Brown AJ Expression and regulation of sterol 27-hydroxylase (CYP27A1) in human macrophages: a role for RXR and PPARγ ligands. Biochem. J 385, 823–830 (2005). [PubMed: 15533057]
24. Leesnitzer LM et al. Functional consequences of cysteine modification in the ligand binding sites of peroxisome proliferator activated receptors by GW9662. Biochemistry 41, 6640–6650 (2002). [PubMed: 12022867]
25. Lugrin J & Martinon F The AIM2 inflammasome: sensor of pathogens and cellular perturbations. Immunol. Rev 281, 99–114 (2018). [PubMed: 29247998]
26. Brunette RL et al. Extensive evolutionary and functional diversity among mammalian AIM2-like receptors. J. Exp. Med 209, 1969–1983 (2012). [PubMed: 23045604]
27. Schattgen SA & Fitzgerald KA The PYHIN protein family as mediators of host defenses. Immunol. Rev 243, 109–118 (2011). [PubMed: 21884171]
28. Hu B. et al. The DNA-sensing AIM2 inflammasome controls radiation-induced cell death and tissue injury. Science 354, 765–768 (2016). [PubMed: 27846608]
29. Shi J. et al. Cleavage of GSDMD by inflammatory caspases determines pyroptotic cell death. Nature 526, 660–665 (2015). [PubMed: 26375003]
30. Ding J. et al. Pore-forming activity and structural autoinhibition of the gasdermin family. Nature 535, 111–116 (2016). [PubMed: 27281216]
31. Edgeworth JD, Spencer J, Phalipon A, Griffin GE & Sansonetti PJ Cytotd interleukinoxicity an-1β processing following Shigella flexneriinfection of human monocyte-derived dendritic cells.Eur. J. Immunol 32, 1464–1471 (2002). [PubMed: 11981835]
32. Bergsbaken T, Fink SL & Cookson BT Pyroptosis: host cell death and inflammation. Nat. Rev. Microbiol 7, 99–109 (2009). [PubMed: 19148178]
33. Miao EA, Rajan JV & Aderem A Caspase-1-induced pyroptotic cell death. Immunol. Rev 243, 206–214 (2011). [PubMed: 21884178]
34. Levine B, Kalman J, Mayer L, Fillit HM & Packer M Elevated circulating levels of tumor necrosis factor in severe chronic heart failure. N. Engl. J. Med 323, 236–241 (1990). [PubMed: 2195340]
35. Testa M. et al. Circulating levels of cytokines and their endogenous modulators in patients with mild to severe congestive heart failure due to coronary artery disease or hypertension. J. Am. Coll. Cardiol 28, 964–971 (1996). [PubMed: 8837575]
36. Torre-Amione G. et al. Proinflammatory cytokine levels in patients with depressed left ventricular ejection fraction: a report from the Studies of Left Ventricular Dysfunction (SOLVD). J. Am. Coll. Cardiol 27, 1201–1206 (1996). [PubMed: 8609343]
37. Chung ES et al. Randomized, double-blind, placebo-controlled, pilot trial of infliximab, a chimeric monoclonal antibody to tumor necrosis factor-α, in patients with moderate-to-severe heart failure: results of the anti-TNF Therapy Against Congestive Heart Failure (ATTACH) trial. Circulation 107, 3133–3140 (2003). [PubMed: 12796126]
38. Mann DL et al. Targeted anticytokine therapy in patients with chronic heart failure: results of the Randomized Etanercept World-wide Evaluation (RENEWAL). Circulation 109, 1594–1602 (2004). [PubMed: 15023878]
39. Everett BM et al. Anti-inflammatory therapy with canakinumab for the prevention of hospitalization for heart failure. Circulation 139, 1289–1299 (2019). [PubMed: 30586730]
40. Bujak M. et al. Interleukin-1 receptor type I signaling critically regulates infarct healing and cardiac remodeling. Am. J. Pathol 173, 57–67 (2008). [PubMed: 18535174]
41. Bageghni SA et al. Fibroblast-specific deletion of interleukin-1 receptor-1 reduces adverse cardiac remodeling following myocardial infarction. JCI Insight 10.1172/jci.insight.125074 (2019).

42. Zeng C. et al. NLRP3 inflammasome-mediated pyroptosis contributes to the pathogenesis of non-ischemic dilated cardiomyopathy. Redox Biol. 34, 101523 (2020). [PubMed: 32273259]
43. Gulick T, Chung MK, Pieper SJ, Lange LG & Schreiner GF Interleukin 1 and tumor necrosis factor inhibit cardiac myocyte β-adrenergic responsiveness. Proc. Natl Acad. Sci. USA 86, 6753–6757 (1989). [PubMed: 2549546]
44. Yokoyama T. et al. Cellular basis for the negative inotropic effects of tumor necrosis factor-α in the adult mammalian heart. J. Clin. Invest 92, 2303–2312 (1993). [PubMed: 8227345]
45. Yu X, Kennedy RH & Liu SJ JAK2/STAT3, not ERK1/2, mediates interleukin-6-induced activation of inducible nitric-oxide synthase and decrease in contractility of adult ventricular myocytes. J. Biol. Chem 278, 16304–16309 (2003). [PubMed: 12595539]
46. Murphy SP, Kakkar R, McCarthy CP & Januzzi JL Jr. Inflammation in heart failure: JACC state-of-the-art review. J. Am. Coll. Cardiol 75, 1324–1340 (2020). [PubMed: 32192660]
47. Noutsias M, Pauschinger M, Schultheiss H & Uwe KH Phenotypic characterization of infiltrates in dilated cardiomyopathy—diagnostic significance of T-lymphocytes and macrophages in inflammatory cardiomyopathy. Med Sci. Monit 8, CR478–CR487 (2002). [PubMed: 12118194]
48. King KR et al. IRF3 and type I interferons fuel a fatal response to myocardial infarction. Nat. Med 23, 1481–1487 (2017). [PubMed: 29106401]
49. Ridker PM Hyperlipidemia as an instigator of inflammation: inaugurating new approaches to vascular prevention. J. Am. Heart Assoc 1, 3–5 (2012). [PubMed: 23130112]
50. Duewell P. et al. NLRP3 inflammasomes are required for atherogenesis and activated by cholesterol crystals. Nature 464, 1357–1361 (2010). [PubMed: 20428172]
51. Seiler SE et al. Obesity and lipid stress inhibit carnitine acetyltransferase activity. J. Lipid Res 55, 635–644 (2014). [PubMed: 24395925]
52. Angelini A. et al. PHDs/CPT1B/VDAC1 axis regulates long-chain fatty acid oxidation in cardiomyocytes. Cell Rep. 37, 109767 (2021). [PubMed: 34610308]
53. Mao H. et al. Endothelium-specific depletion of LRP1 improves glucose homeostasis through inducing osteocalcin. Nat. Commun 12, 5296 (2021). [PubMed: 34489478]
54. Bray NL, Pimentel H, Melsted P & Pachter L Near-optimal probabilistic RNA-seq quantification. Nat. Biotechnol 34, 525–527 (2016). [PubMed: 27043002]
55. Love MI, Huber W & Anders S Moderated estimation of fold change and dispersion for RNA-seq data with DESeq2. Genome Biol. 15, 550 (2014). [PubMed: 25516281]
56. Shi JW & Walker MG Gene set enrichment analysis (GSEA) for interpreting gene expression profiles. Curr. Bioinform 10.2174/157489307780618231 (2007).
57. Wolf FA, Angerer P & Theis FJ SCANPY: large-scale single-cell gene expression data analysis. Genome Biol. 10.1186/s13059-017-1382-0 (2018).
58. Virtanen P. et al. SciPy 1.0: fundamental algorithms for scientific computing in Python. Nat. Methods 17, 261–272 (2020). [PubMed: 32015543]
59. Amara CS et al. Serum metabolic profiling identified a distinct metabolic signature in bladder cancer smokers: a key metabolic enzyme associated with patient survival. Cancer Epidemiol. Biomark. Prev 28, 770–781 (2019).
60. Vantaku V. et al. Large-scale profiling of serum metabolites in African American and European American patients with bladder cancer reveals metabolic pathways associated with patient survival. Cancer 125, 921–932 (2019). [PubMed: 30602056]
61. Louch WE, Sheehan KA & Wolska BM Methods in cardiomyocyte isolation, culture, and gene transfer. J. Mol. Cell. Cardiol 51, 288–298 (2011). [PubMed: 21723873]

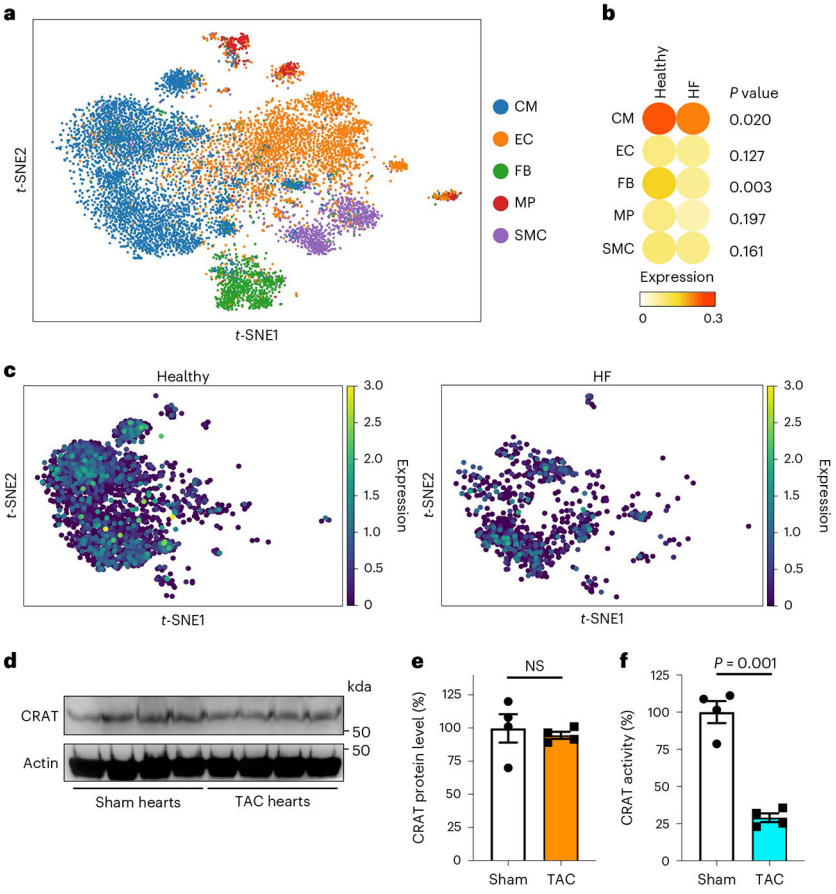

Fig. 1 |. CRAT is downregulated in patients with HF and its activity is decreased in a mouse model of HF induced by transaortic constriction.

a, *t*-SNE plot showing 9,248 single cells isolated from hearts from both healthy individuals and patients with HF. **b**, CRAT expression in both CMs and FBs from patients with HF was significantly downregulated. CMs, $P = 0.020$; FBs, $P = 0.003$; Wilcoxon rank-sum test, one-sided test. EC, endothelial cell; SMC, smooth muscle cell. **c**, *t*-SNE plot of CMs from hearts of healthy individuals and patients with HF. The color indicates the expression level of CRAT. **d**,**e**, Western blots and quantification analysis indicated that CRAT protein level was not changed in male and female mouse hearts at 4 weeks after TAC operation. **f**, CRAT activity was dramatically decreased in TAC hearts. $n = 4$ mice (**e**,**f**) per group. Data are presented as mean ± s.e.m. NS, not significant. Analysis was carried out by unpaired two-tailed Student's *t*-test (**e**,**f**).

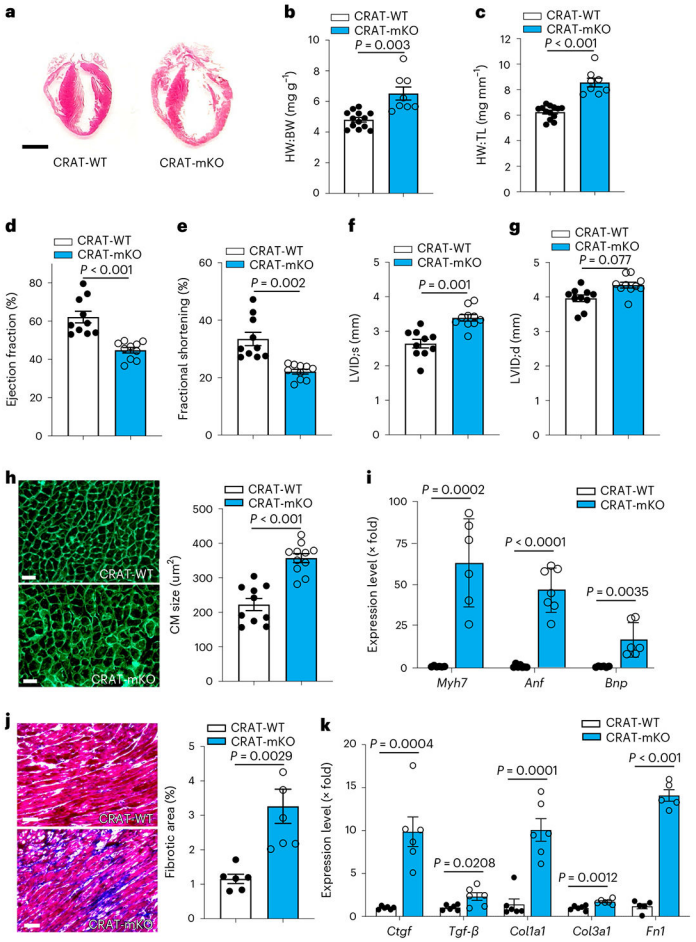

Fig. 2 |. Cardiomyocyte-specific deletion of CRAT leads to dilated cardiomyopathy in mice. Adult *Crat* (flox/flox); Myh6-Cre$^{\pm}$ male and female mice were injected with tamoxifen for 4 d consecutively to specifically delete CRAT in CMs. **a**, Representative images of four-chamber heart sections stained with hematoxylin and eosin. Scale bar, 2 mm. **b**,**c**, HW:BW and HW:TL ratios were calculated at 2 months after tamoxifen injection. **d**–**g**, Echocardiographic analyses indicated that deletion of CRAT in CMs impaired cardiac contractile function and resulted in DCM. LVID;s, left ventricular internal diameter end systole; LVID;d, left ventricular internal diameter end diastole. **h**, Representative images of WGA staining and quantitative analysis of CM cross sectional size. Scale bar, 25 μm. **i**, RT–PCR analysis of the expression of the hypertrophy marker genes in the hearts of CRAT-mKO mice and control WT mice. **j**, Representative pictures of Masson's trichrome staining of cardiac sections and quantitative analysis of fibrotic area. Scale bar, 50 μm. **k**, RT–PCR analysis of the expression of the pro-fibrotic genes in the hearts of CRAT-mKO and WT mice. *n* = 13 mice (**b**,**c**, WT), 8 mice (**b**,**c**, mKO), 10 mice (**d**–**g**), 10 mice (**h**, WT), 11 mice (**h**, mKO), 6 mice (**i**, *Myh7, Bnp*), 7 mice (**i**, *Anf*), 6 mice (**j**, WT), 7 mice (**j**, mKO), 6 mice (**k**, *Ctgf, Tgf-b, Collal, Col3a1*), 5 mice (**k**, *Fn1*) per group. Data are presented as mean ± s.e.m. Analysis was carried out by unpaired two-tailed Student's *t*-test (**b**–**k**).

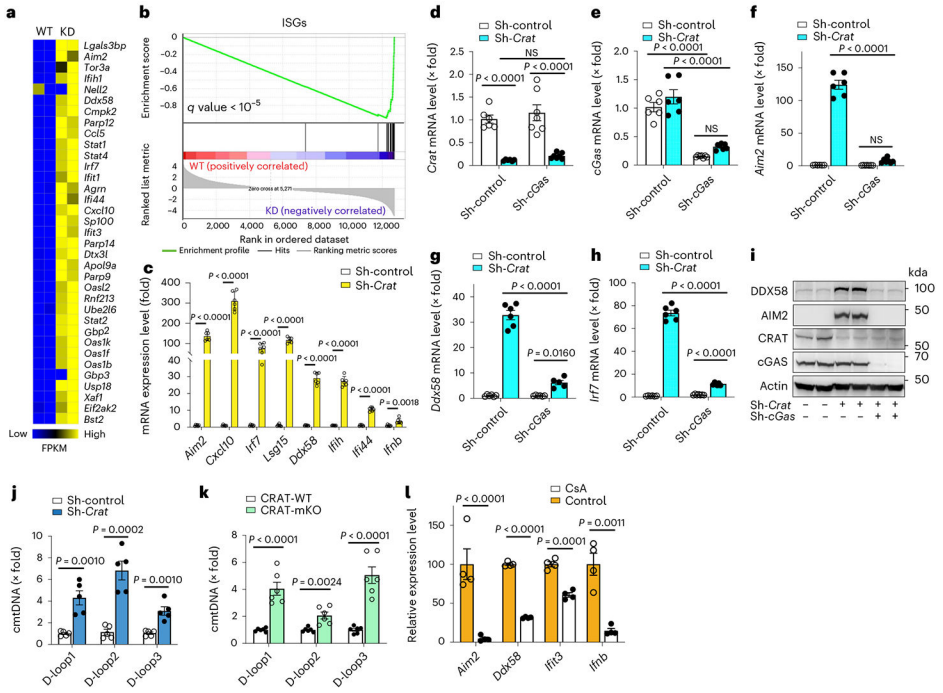

Fig. 3 | Depletion of CRAT triggers type I interferon responses in primary cardiomyocytes. **a**,**b**, Heat map and GSEA of ISGs in NRVMs transduced with lentivirus expressing control shRNA (WT) or *Crat* shRNA (KD). **c**, RT–PCR confirmed the induction of ISGs in CRAT-deficient NRVMs. **d**–**h**, RT–PCRs indicated that increased expression of ISGs in CRAT-deficient NRVMs was dependent on cGAS. **i**, Western blots confirmed cGAS-dependent induction of some ISGs in CRAT-deficient NRVMs.**j**, Quantification of cytosolic mtDNA in control or CRAT-deficient NRVMs. **k**, Quantification of cytosolic mtDNA in adult CMs isolated from CRAT-WT or CRAT-mKO male and female hearts. **l**, Treatment with cyclosporin A (CsA, 10 μM) significantly inhibited ISG expression in CRAT-deficient NRVMs. $n = 6$ (**c**), $n = 6$ (**d**–**h**, Sh-control), $n = 7$ (**d**–**f**,**h**, Sh-*cGas*), $n = 5$ (**g**, Sh-*cGas* and Sh-*Crat*), $n = 5$ (**j**), $n = 6$ (**k**) and $n = 4$ (**l**) biologically independent samples per group. Data are presented as mean ± s.e.m. Analysis was carried out by two-way analysis of variance (ANOVA) followed by Bonferroni's multiple comparison test (**d**–**h**) and unpaired two-tailed Student's *t*-test (**c**,**j**–**l**).

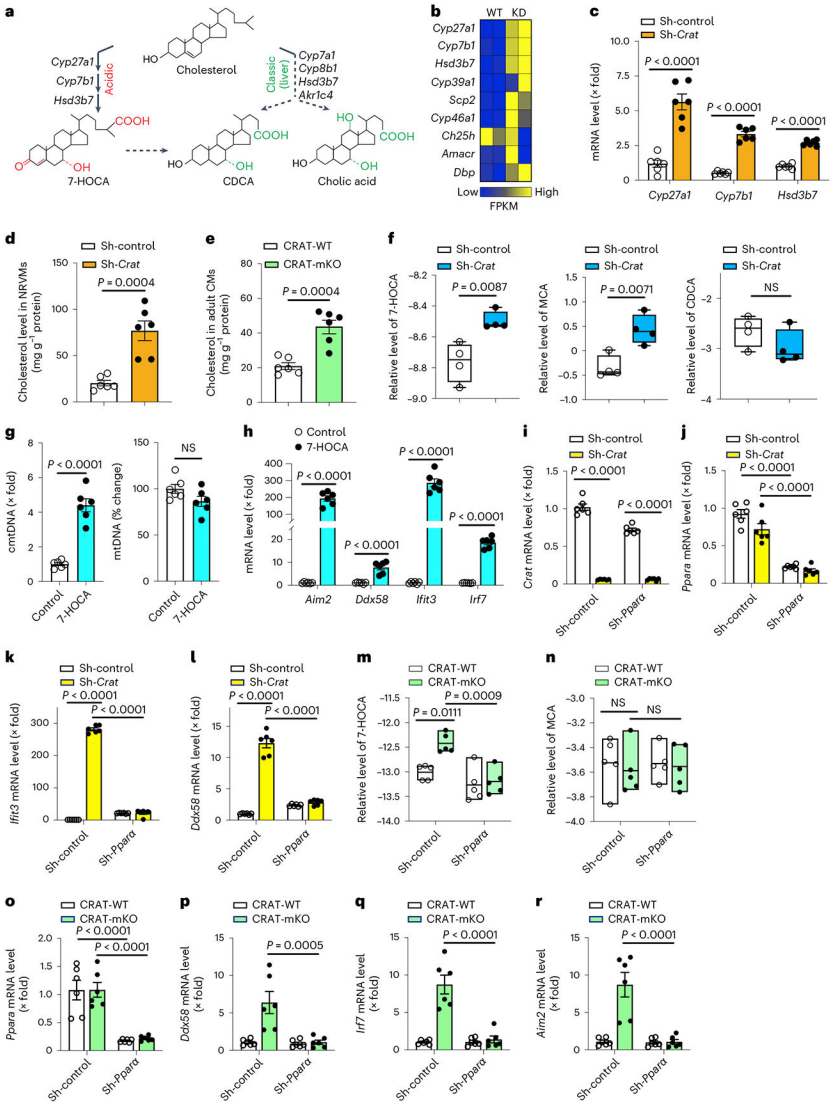

Fig. 4 |. Bile acid synthesis intermediate 7-HOCA promotes mtDNA stress and induces ISG expression.

a, Schematic diagram of the classic and acidic bile acid synthesis pathways. **b**, Heat map analysis of the major enzymes of bile acid synthesis pathway expressed in NRVMs. **c**, RT–PCR confirmed the increased expression of *Cyp27a1*, *Cyp7b1* and *Hsd3b7* in CRAT-deficient NRVMs. **d**,**e**, Cholesterol level was increased in CRAT-deficient NRVMs (**d**) and adult CMs isolated from CRAT-mKO male and female mice (**e**). **f**, Metabolomics analysis indicated intracellular accumulation of 7-HOCA and MCA in CRAT-deficient NRVMs. **g**,**h**, 7-HOCA (100 μM) induced mtDNA release into cytosol (**g**) and ISG expression (**h**) in NRVMs after 24 h of treatment. **i**–**l**, Knockdown of PPARα abolished the increase in ISG expression induced by CRAT depletion in NRVMs. **m**–**r**, Adult CRAT-WT and CRAT-mKO male and female mice were injected with AAV9-sh-control or AAV9-sh-*Pparα* virus (5×10^{11} GC per mouse) at 1 week before tamoxifen administration. Four weeks later, CMs were isolated for metabolomics analysis and RT–PCR. Knockout of CRAT led to an increase in 7-HOCA (**m**) and ISG expression in vivo (**o**–**r**), which are dependent on PPARα. $n = 6$

biologically independent samples (**c**,**d**,**g**–**l**), $n = 6$ mice (**e**), $n = 4$ biologically independent samples (**f**), $n = 5$ mice (**m**,**n**) and $n = 6$ mice (**o**–**r**) per group. Data are shown as the mean ± s.e.m. (**c**–**e**,**g**–**l**,**o**–**r**). The black line inside the box plots (**f**,**m**–**n**) represents the median value and the size of the box is determined by the 25th and 75th percentiles of the data. The whiskers of the box plot represent the maximum and minimum values of the data. Analysis was carried out by unpaired two-tailed Student's *t*-test (**c**–**h**) and two-way ANOVA followed by Bonferroni's multiple comparison test (**i**–**r**).

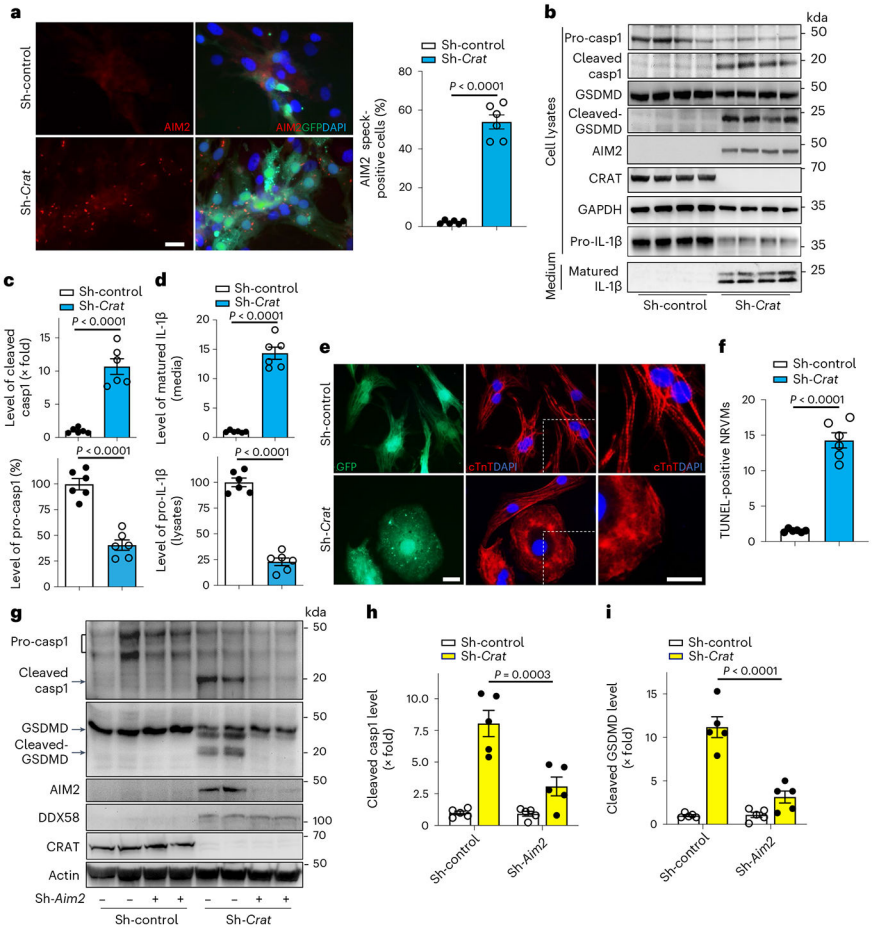

Fig. 5 | Depletion of CRAT activates DNA-sensing AIM2 inflammasome.

NRVMs were transduced with lentivirus expressing control shRNA or *Crat* shRNA for 5 d. All transduced cells expressed green fluorescent protein (GFP). **a**, Cells were fixed for immunostaining with anti-AIM2 antibody. Representative images showed that knockdown of CRAT induced the formation of AIM2 specks. Scale bar, 25 μm. **b**–**d**, Western blots and quantification analyses indicated that the cleavage of pro-caspase-1 (**c**) and pro-IL-1β (**d**) was increased in CRAT-deficient NRVMs. **e**, Representative images of NRVMs stained with cardiac troponin-T antibody showed that knockdown of CRAT disrupted sarcomere organization. Scale bar, 25 μm. **f**, Depletion of CRAT significantly increased the number of TUNEL-positive NRVMs. **g**–**i**, Western blots confirmed that AIM2 was required for pro-caspase-1 and GSDMD cleavage in CRAT-deficient NRVMs. $n = 6$ (**a**,**c**,**d**,**f**) and $n = 5$ (**h**,**i**) biologically independent samples per group. Data are shown as mean ± s.e.m. Analysis was carried out by unpaired two-tailed Student's *t*-test (**a**,**c**,**d**,**f**) and two-way ANOVA followed by Bonferroni's multiple comparison test (**h**,**i**).

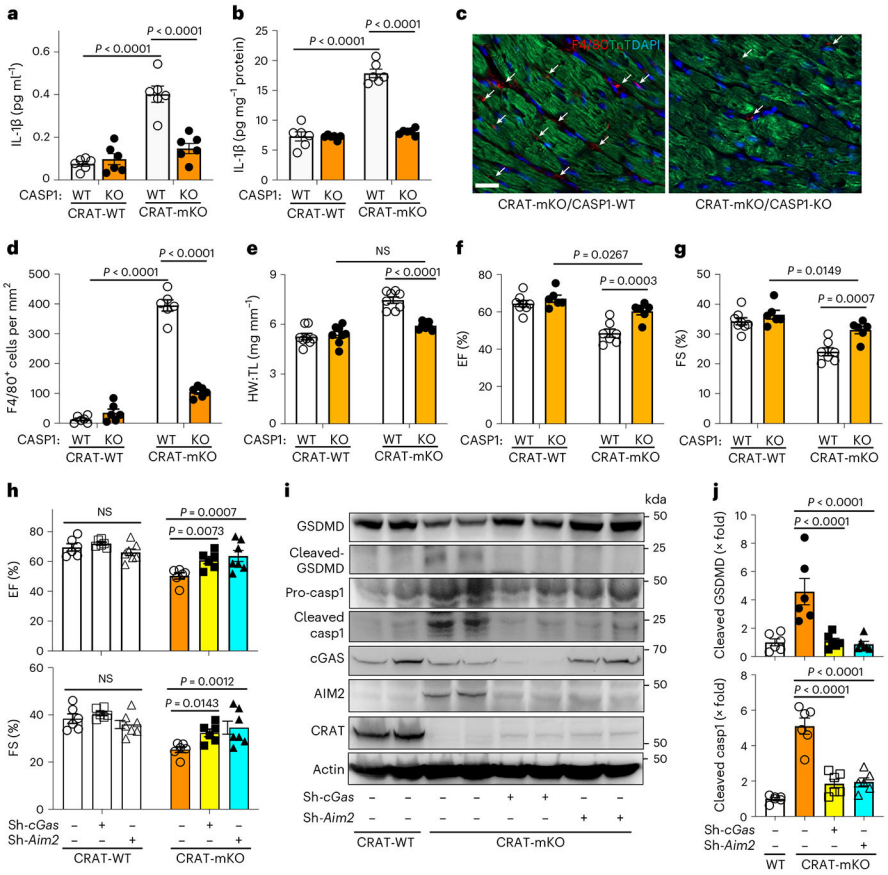

Fig. 6 | Depletion of caspase-1, cGAS or AIM2 reverses myocardial inflammation and dilated cardiomyopathy induced by CRAT knockout.

a,**b**, Combined deletion of caspase-1 In CRAT-mKO male and female mice inhibited the increases in IL-1β level in serum (**a**) and hearts (**b**). **c**,**d**, Representative images and quantitative analysis showed that the infiltration of F4/80^{+} macrophages in CRAT-mKO male and female hearts was significantly inhibited by combined deletion of caspase-1. Scale bar, 25 μm. DAPI, 4,6-diamidino-2-phenylindole. **e**–**g**, HW:TL ratios (**e**) and echocardiographic analyses (**f**,**g**) at 2 months after tamoxifen injection indicated that combined deletion of caspase-1 reversed the compromised cardiac function induced by CRAT deficiency. EF, ejection fraction; FS, fractional shortening. **h**–**j**, CRAT-WT and CRAT-mKO male and female mice were injected with AAV9-sh-control, AAV9-sh-cGas or AAV9-sh-*Aim2* virus (5×10^{11} GC per mouse) at 1 week before tamoxifen administration. After 8 weeks, echocardiographic analyses were performed to evaluate cardiac contractile function (**h**). CMs were then isolated for western blots to examine the roles of cGAS and AIM2 in inflammasome activation induced by CRAT depletion in vivo (**i**,**j**). $n = 6$ (**a**,**b**,**d**), $n = 8$ (**e**), $n = 7$–8 (**f**,**g**, WT), $n = 6$ (**f**,**g**, Casp1 KO), $n = 6$ (**h**, WT, Sh-*cGas*), $n = 7$ (**h**, Sh-*Aim2*) and $n = 6$ (**j**) mice per group. Data are shown as mean ± s.e.m. Analysis was carried out by two-way ANOVA followed by Fisher's LSD multiple comparison test (**a**,**b**,**d**–**g**,**h**,**j**).

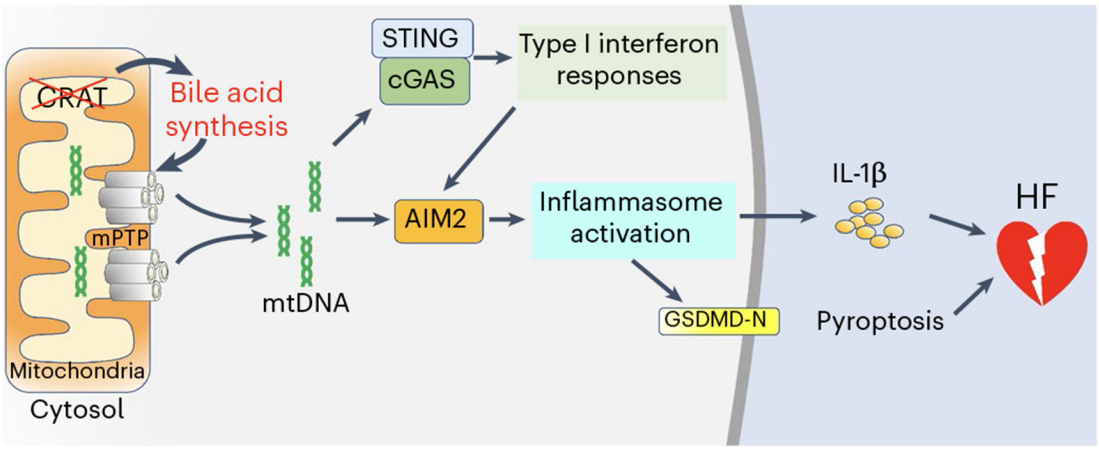

Fig. 7 |. Schematic model of the role of CRAT in cholesterol metabolism and innate immune responses.

Loss of CRAT promotes cholesterol catabolism through the bile acid synthesis pathway, leading to intracellular accumulation of intermediates of bile acid synthesis such as 7-HOCA, which is sufficient to promote mtDNA release into cytosol and trigger cGAS–STING-dependent type I interferon responses. Further, type I interferon responses elicited by CRAT deficiency lead to a substantial increase in AIM2 expression and subsequent activation of the DNA-sensing AIM2 inflammasome, which in turn promotes proteolytic maturation of IL-1β and CM pyroptosis. Eventually, genetic deletion of CRAT in CMs leads to myocardial inflammation and results in DCM. Collectively, we have identified a mechanism by which cardiac energy metabolism, cholesterol homeostasis and CM-intrinsic innate immune responses are interconnected via a CRAT-mediated bile acid synthesis pathway, which contributes to chronic myocardial inflammation and HF progression.